STUDY OF MAGNETIC MOTIONS IN THE SOLAR PHOTOSPHERE AND THEIR IMPLICATIONS FOR HEATING THE SOLAR ATMOSPHERE

NASA Grant NAGW-2545

Annual Reports No. 2 and 3

For the period 1 June 1993 through 31 May 1995

Principal Investigator

Robert W. Noyes

July 1995

Prepared for

National Aeronautics and Space Administration

Washington, D.C. 20546

Smithsonian Institution
Astrophysical Observatory
Cambridge, Massachusetts 02138

The Smithsonian Astrophysical Observatory
is a member of the
Harvard-Smithsonian Center for Astrophysics

The NASA Technical Officer for this Grant is Dr. William J. Wagner, Solar Physics Branch, Space Physics Division, Code SS, NASA Headquarters, Washington, D.C. 20546

NASA Grant NAGW-2545
Study of Magnetic Structure in the Solar Photosphere and Chromosphere

1 Introduction

This progress report covers the first year of NASA Grant NAGW-2545, a Study of Magnetic Structure in the Solar Photosphere and Chromosphere. We have made very significant progress in three areas: (1) analysis of vorticity in photospheric convection, which probably affects solar atmospheric heating through the stresses it imposes upon photospheric magnetic fields, (2) modelling of the horizontal motions of magnetic footpoints in the solar photosphere using an assumed relation between brightness and vertical motion as well as continuity of flow, and (3) observations and analysis of infrared CO lines formed near the solar temperature minimum, whose structure and dynamics also yield important clues to the nature of heating of the upper atmosphere. Here we summarize our progress in each of these areas in turn. In Appendix I, we provide a progress report for the work carried out under the SPEO supplement to this grant. Appendix II provides copies of papers prepared or published this year with support from the grant.

2 Vorticity and Divergence in the Solar Photosphere

Motions of magnetic footpoints in the photosphere are thought to be closely related to heating of the upper solar atmosphere. It is now well-established that these motions result from bodily transport of predominantly vertical magnetic field lines by the horizontal component of turbulent convection: magnetic flux knots are swept to granule, mesogranule, and supergranule boundaries, and collect in regions of converging flow at the vertices of mesogranules and supergranules. In converging flow, if there is a net angular velocity, conservation of momentum leads to a significant vorticity in the flow. Contrariwise, for diverging flow (e.g. outflow from a local source of upwelling material) conservation of angular momentum should cause the vorticity to decrease.

We have explored these ideas through analysis of an excellent series of photospheric observations obtained from Pic du Midi observatory, supplemented by observations from the Swedish Solar Telescope at La Palma. We calculated the horizontal vector flow field using a correlation tracking algorithm, and from this derived three scalar fields: the horizontal flow speed, the divergence of the flow, and the vertical component of the curl of the flow. We found that the divergence of the flow has more power and greater lifetime than does the curl: that is, episodes of inflow or outflow are longer-lived and greater in amplitude than episodes of significant curl or vorticity. The largest values of divergence are statistically found in regions where the horizontal flow speed is largest; we associate these regions with exploding granules. Regarding the relation between vorticity and divergence, as predicted the highest vorticity is statistically associated with areas of negative divergence, i.e. with converging flow, such as intergranular lanes or verticies of granular, mesogranular, and supergranular

flow. The effect is not large, but it is statistically very significant. A study of the flowfields in a numerical simulation of convection shows a similar dependence of vorticity on divergence. so this would seem to be a general property of convection.

All of the above conclusions result from a statistical analysis. We also sought examples where we could see visual evidence of strong vorticity in the granulation flow. Somewhat to our surprise, only rarely did we find events with vorticity strong enough to dominate the random component of the turbulent flow; one such event however had a remarkably large circulation velocity, of 3 km/s around a radius of 450 km; this corresponds to one rotation every 1000 seconds.

This research, carried out together with Harvard undergraduate student Wang Yi, has been published in the July 1995 issue of Astrophysical Journal (Wang, Noyes. Tarbell. and Title 1995; see also Appendix II).

3 Flowfield Modelling

Sequences of G-band images taken at the Swedish Solar Telescope at La Palma show small. bright features in the intergranular lanes which are thought to be the signatures of magnetic flux tubes. These features are seen quite clearly in the best quality frames but fade in and out due to atmospheric seeing. One of us (Nisenson) has been applying our technique of blind iterative deconvolution to improve the resolution in the poorer images, allowing tracking of these features over extended time periods. We have also developed digital filtering techniques which allow automated identification of these features so that we can track individual features or groups of features over a long sequence of frames. We have worked with a sequence of 187 frames taken on an 8 second cadence (the best frame in each 8 second interval is selected). We have found that very few of the bright features are trackable for more than a few frames. The longest lived of these lasts only a few minutes and the brightness of the feature varies considerably over that time. However. if one groups together the positions of bright features over much longer time intervals, relatively stable patterns emerge whose spatial scale is several times that of the granulation scale (on the order of 10 arcseconds) and these patterns appear to be stable over periods longer than the granulation overturn time.

We wished to compare the dynamics of these measurements to models of the granulation. In order to do this, we need to measure the flowfield velocities from the actual data. While this can be done with "correlation tracking", we have been testing a complementary technique (suggested by co-investigator van Ballegooijen), which may provide higher angular resolution than correlation tracking. With this technique we may derive the flowfield velocity directly from the intensity and its gradient at a single point, rather than by averaging the correlation over an extended area to derive the velocity at the center of the area. The key is to note that brighter-than-average areas are generally regions of upflow and hence (by continuity) horizontal outflow; the direction of outflow should be along the direction of intensity gradient (from brighter to fainter). To apply this concept. we first filter the images to reduce the effect of the small, high-frequency features such as

intergranular lanes on the calculated gradients. Then we set the horizontal velocity to the spatial gradient of the filtered image, with a scale factor set to agree with the results from large-scale correlation tracking.

As a test of the method, we have inserted test-particles, or "corks" randomly in the granulation intensity field and traced their motions as determined by the time-varying intensity gradients in successive images. Importantly, we have demanded that the "corks" have finite size–that is, they cannot approach arbitrarily closely to each other; this mimics the resistance of magnetic flux elements to compression beyond a minimum size determined by the maximum magnetic flux density. Figure 1 shows the result after calculations for 171 successive frames, after inserting such corks randomly in the first of the frames. The results are qualitatively remarkably similiar to the bright magnetic features seen in the G band in La Palma data. The corks distribute themselves in a relatively stable pattern with characteristic scale of a few granules. The pattern seems to remain unchanged at later times, but the corks become even more densely clustered.

We are now attempting to compare the calculated "cork" positions with the actual evolution of bright elements in a data set of La Palma G-band images, to see if the magnetic elements do indeed follow the motions predicted by the simple algorithm described above. Publication is in preparation (Nisenson et al 1995).

4 Imaging spectroscopy of the solar CO lines at 4.67μm

Not many spectral diagnostics are available to study the structure and dynamics of the solar chromosphere. Our knowledge stems mostly from a few strong lines like the hydrogen Hα and Ca II H&K lines, while most other lines have chromospheric contributions only close to the limb where foreshortening makes observations difficult. Due to this lack of reliable observations we are currently not even exactly certain of the nature of the chromosphere. and what processes cause its temperature to rise from photospheric to (eventually) coronal values. Recent simulations by Carlsson & Stein (1995, ApJ 440, L29-L32) suggest that the chromo"sphere" need not exist over the whole surface but rather represents moderately hot material that is locally and intermittently heated by outwardly propagating shock waves. With this in mind it is evident that we need to look for new observations that could confirm or reject such new models that are widely different from, more traditional, plane-parallel hydrostatic ones. It may seem unlikely that observations of molecular carbon monoxide (CO) lines provide us with such an opportunity, since all molecules dissociate at temperatures precisely characteristic of the chromosphere. However, in the case of the solar chromosphere we are particularly interested in the amount of mechanical energy coming from the chromosphere's lower boundary, ie., the temperature minimum region. Lines of CO may play an important role in diagnosing this energy flux and the form in which it is presented to the chromosphere.

In a static plane-parallel solar model both the balance of CO association and dissociation and the excitation–de-excitation equilibrium of the vibration-rotation transitions are dominated by collisions (Ayres & Wiedemann 1989, ApJ, 338, 1033-1046). Consequently.

all relevant populations are in thermodynamic equilibrium with local conditions (LTE), and intensities map directly into temperatures. Surprisingly enough, CO observations close to the limb require temperatures as low as 3700—3800 K, values which are much lower than those predicted by models based on almost any other spectral diagnostic. A recently constructed model by co-investigator E. H. Avrett (see Appendix II) illustrates the discrepancy in thermal diagnostics clearly. The model fits disk-center intensities of several hundred CO lines in the ATMOS infrared atlas (Farmer & Norton 1989, NASA Ref. Publ. 1224, Vol. 1) but predicts intensities that are far too low in such prominent spectral features as the Ca II H&K lines and the 150 nm and 100 μm continua which both originate from the same region. This failure of standard one-dimensional models to accommodate CO observations with other spectral diagnostics clearly calls for more intricate models of the solar atmosphere that include spatial inhomogeneities and/or time-dependent behavior. For this we need detailed observations that show when and where in the atmosphere the lowest CO temperatures occur.

Observations

In October 1993 and May 1994 we had the opportunity to observe the fundamental rotation-vibration lines of CO at 4.67μm at the National Solar Observatory of Kitt Peak. We used the infrared grating of the 13.8-m vertical spectrograph on the 1.5-m main telescope of the McMath–Pierce facility to obtain high-resolution ($\nu/\Delta\nu \approx 90\,000$) spectra of the CO lines in the atmospheric window around 2143 cm^{-1} (4.67 μm). A narrowband filter was used to isolate the second order, for which the theoretical diffraction-limited resolving power is 110 000. Spectra were recorded with a 256×256 InSb array camera (Amber Engineering) behind minifying transfer optics. This setup imaged a 2.5 cm^{-1} portion of the spectrum on the detector. The 250 μm-wide slit subtended an area of 0.″63×51″ (October 1993) or 0.″63×100″ (May 1994) on the Sun. Since the diffraction limited resolution of the telescope is 0.″77 at 4.67 μm, this oversamples the spectrum perpendicular to the dispersion.

Addition of an optical disk in May 1994 increased data throughput of the system resulting in a cadence of 2 seconds per frame, an improvement of more than a factor of 2 over the first observations in October 1993. During the second observing run we also had the added capability to take Ca II K-line images co-spatial with the slit position of the infrared spectrograph.

We used the instrument in two different modes of observation: one that stressed resolution in space, the other resolution in time. In the first mode we scanned the solar surface with the spectrograph slit to build spectra-spectroheliograms, data cubes that allow us to make two-dimensional spatial maps of any function of wavelength such as the intensity in a stretch of continuum, the core of a certain line, or a line's Doppler shift. In the second mode we took time-sequences of spectra at a fixed position on the surface and recorded temporal variations of spectral quantities along the slit.

During this first year of the present grant we have carried out a detailed analysis of these data. We subtracted dark frames obtained by exposing with the spectrograph slit closed, and then divided the results by appropriate flat field images. The flat fields were obtained for each sequence by moving the telescope over the solar surface during exposure and averaging

8–12 frames, and then removing the spatially-averaged spectrum by averaging each column of the array (along the slit) and dividing each pixel (spatial location) in that column by the average. Finally, we removed bad pixels from the dark-subtracted and flat-fielded frames by interpolation from neighboring pixels at the same wavelength.

Results The picture of the temperature minimum region that emerges from time and space resolved spectroscopy of the infrared CO lines is a very dynamical one. Our first observations with the infrared array (published in Uitenbroek, Noyes, & Rabin, 1994, ApJ, 432, L67-L70; see Appendix II) showed that, at disk center, line shifts variations have a dominant period of 5 minutes, spatial scales of 10–20″, and typical RMS amplitudes of 0.3–0.4 km/s. Line-core intensities of the stronger lines exhibit more the character of the chromospheric 3-minute oscillations with a smaller spatial scale of 3–5″, and RMS variations that correspond to 90 K temperature fluctuations. Higher up in the temperature minimum region the spatial distribution of temperatures appears asymmetric with an extended tail towards small-scale cold elements. The magnetic network could be tentatively identified (as bright elements) in the intensity maps, but this could not be substantiated since we did not have co-spatial Ca II K line images during the October 1993 run. The network did not seem to have a clear signature in maps of line shift.

Figure 2 shows a time-sequence of brightness (converted to temperature fluctuations) and line-shift variations of the core of the strong CO 3-2 R14 line obtained on May 6, 1994 under very favourable seeing conditions. We have discussed this observation in a second paper (Uitenbroek & Noyes, 1994, in the "Proceeding of the OSLO mini-workshop on Chromospheric Dynamics", held from 6-8 June, 1994 in Oslo, Norway; see Appendix II).

In the displayed time-sequence of Figure 2 we see a fine-scale pattern with structures as small as 1″, that reminds us of the photospheric granulation: bright streaks that last for several minutes and that sometimes diverge, sometimes converge. Since the spectrograph slit renders a one-dimensional cross-section of the solar surface, the streaks most likely represent ring shaped (although not necessarily circular) structures. The typical separation of 3-5″of the bright streaks is slightly larger than the cell size of photospheric granulation, but corresponds perhaps to the strongest granules overshooting in the stable temperature minimum region These appear as "exploding" granules in photospheric granulation movies. In between the bright streaks there are sometimes dark single streaks that last for about 2 minutes. These intermediate dark narrow elements are among the darkest elements in the time-sequence, reminiscent of the centers of large granules that cool strongly due to the adiabatic expansion of upflowing material in the exponentially stratified atmosphere in theoretical granulation simulations.

Looking at the results from our two observing runs we get the strong impression that the dark CO line cores observed close to the solar limb are mainly dynamical in origin. It seems there are no locations in the solar atmosphere that are preferentially cool all the time. Rather our observations seem to indicate that the coolest elements seen at any time on the surface are temporary in nature, and probably related to instances of strong granular overshoot.

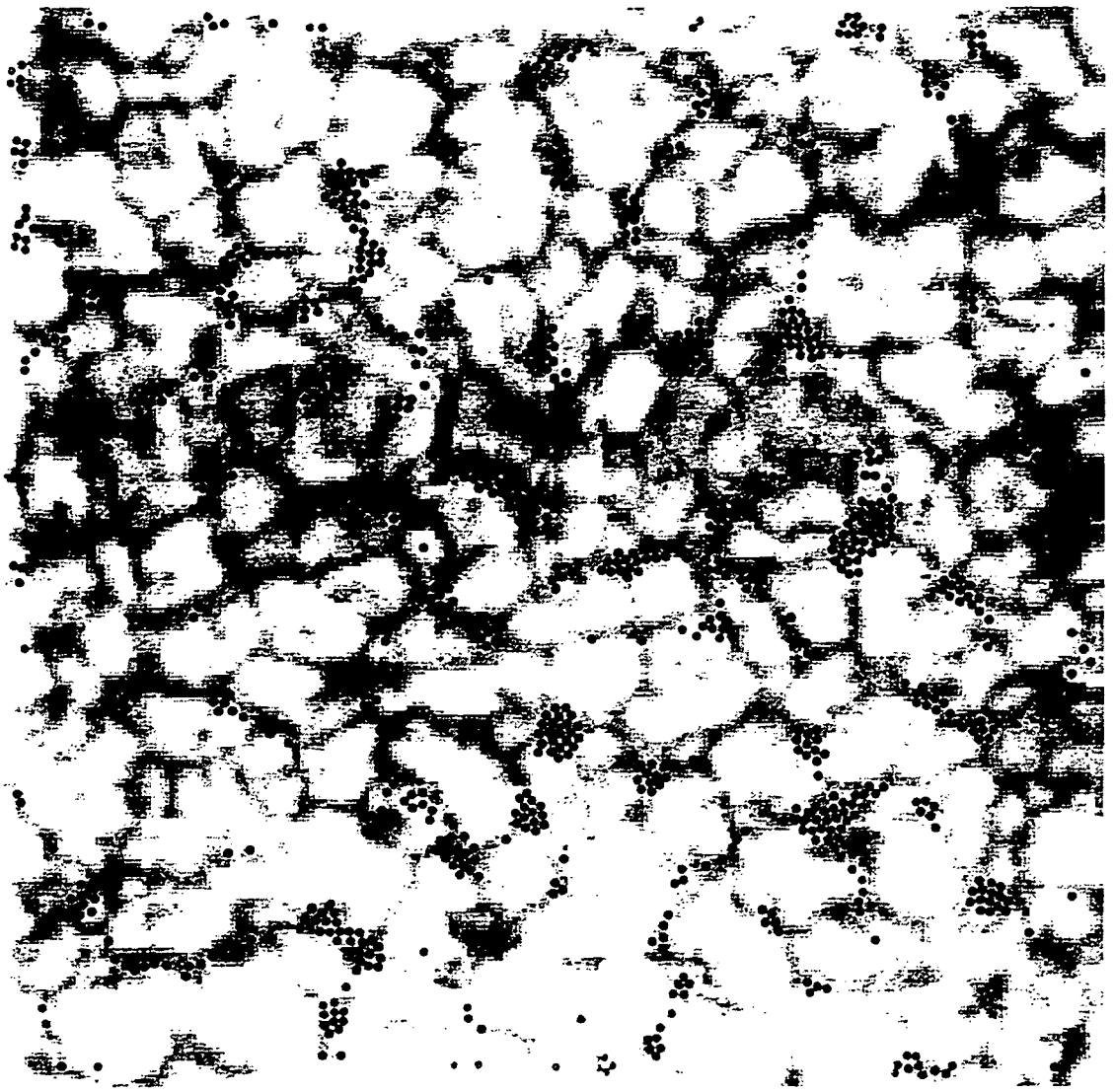

Figure 1. The position of initially randomly placed "corks" in the solar photosphere after transport by horizontal flowfields as calculated for a 57-minute sequence (172 frames) of Pic du Midi data, using the intensity gradient method described in the text. Shown in the background is the granulation pattern of the last image.

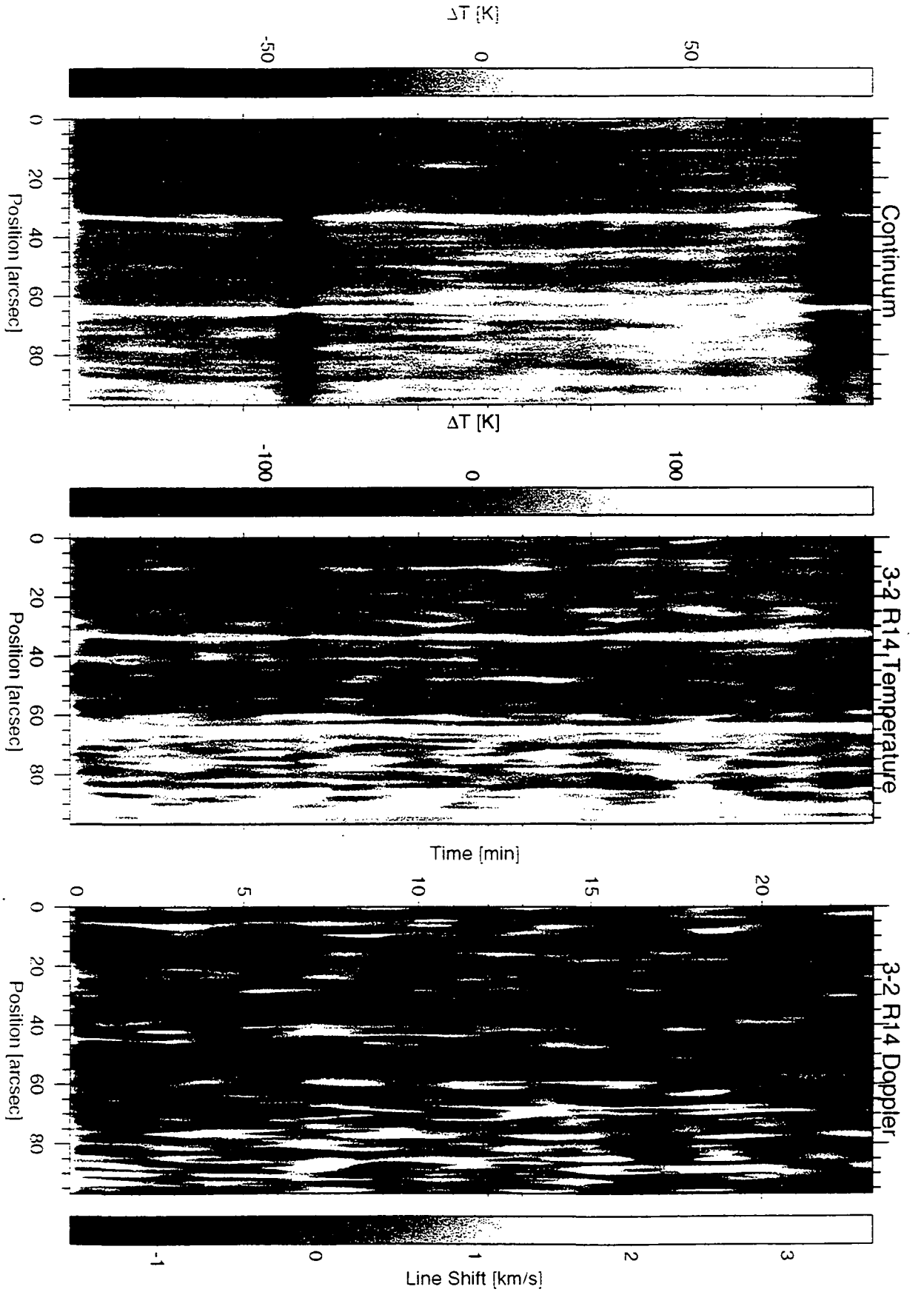

Figure 2. Space-time maps of infrared continuum variation (left panel), CO 3-2 R14 line-core temperature (middle panel), and Doppler shift variation in the same spectral line (right panel). See text for details.

5 Papers prepared under this grant

The following papers prepared with support from this grant were submitted or published during the report period. Copies are attached as Appendix II.

Avrett, E. H. 1995, "Two-component Modeling of the Solar IR CO Lines", proceedings 15th NSO/Sacramento Peak Workshop, *Infrared Tools for Solar Astrophyhsics: What's Next?*. In Press.

Uitenbroek, H., Noyes, R.W., and Rabin, D. 1994, "Imaging Spectroscopy of the Solar CO Lines at 4.67 μm", Ap. J. **432**, L67-70.

Uitenbroek, H., and Noyes, R.W. 1994, "New Insight in the solar Tmin region from the CO lines at 4.67 micron", in *Chromospheric Dynamics*, Proc. OSLO mini-workshop June 1994 (Mats Carlsson, ed), p. 129-138.

Wang,Y., Noyes, R.W., Tarbell, T.D., and Title, A.M. 1995, "Vorticity and Divergence in the Solar Photosphere", Ap.J. **447**, 419-27.

6 APPENDIX I: SPEO Supplement

Report on SPEO supplement activities at the
Maria Mitchell Observatory, Nantucket, MA
Eileen Friel, Director

The SPEO supplement to NASA grant NAGW-2545 has been used to support a variety of solar physics and astronomy programs through the Maria Mitchell Observatory. Programs reach both summer visitors and local Nantucket elementary school children by providing students with an opportunity to explore the concepts of space physics and astrophysics as well as the technology and tools used by astronomers. SPEO supplements provide teacher salary and educational and demonstration equipment.

The Maria Mitchell Observatory is known for its undergraduate research program which introduces college students to independent, supervised research on topics and techniques of current astrophysics. The Observatory is located on Nantucket Island, which in the summer time is a well-known New England resort, and many of the children reached through SPEO sponsored programs are part of the summer tourist population. By contrast, the year-round population of Nantucket is a rural community of about six thousand people who gain their livelihood primarily by fishing, building, trades, and service to the summer residents and tourists. Because of its isolation, the year-round island community lacks many of the opportunities available in a larger urban environment. In the wintertime, Nantucket children are as isolated as any in the United States and the opportunities provided through SPEO funding have been significant to many of them. Though SPEO sponsored activities are designed to reach both the summer tourist population and the local community, we have placed more emphasis on and have had considerably more success with programs for Nantucket children.

Summer astronomy programs offer week-long classes that emphasize demonstrations and hands-on activities and involve students directly with the concepts of astronomy by illustration. Each summer we offer a variety of topics, including those on the Sun, size and scale in the universe, the planets, and the techniques of astronomy with focus on telescopes and the tools astronomers use. Students make observations, for example, using telescopes to image the Sun and spectroscopes to see Fraunhofer lines and elements in the lab, they build model telescopes using optics in the Observatory and scale models to obtain a sense of size and distance in the Universe. The week-long sessions also involve an open night for students and their parents using both historic and modern telescopes at the Observatory. Summer programs tend to attract children of summer residents and visitors and annually reach up to 50 students aged 9 - 12.

However, our fall programs, offered to children in Nantucket Elementary School, have the potential to make a much more permanent impact and provide a more needed service. We have been fortunate to be able to work with an outstanding teacher of a 4th grade class, and with her help are learning how to integrate our astronomy activities effectively in the classroom. In particular, she and other teachers have urged us to integrate math curricular concepts into our astronomy activities - as a result, astronomy now becomes a way of teaching math, and can be fully incorporated into the regular curriculum. We work with small groups of 6 or 7 students at a time, and bring them to the Observatory for a week-long session of 2 hours daily. Taking the students out of the school at times presents logistical problems, but the benefit to the students, and their opportunity to take advantage of the Observatory resources has been one of the high points of our activities. The astronomy activities have been taught by novice teaching interns, who, like our undergraduate research interns, have an opportunity to participate in innovative educational programs in a resource-rich environment.

The week begins with an introduction to a fundamental concept, such as density or temperature, or the scale of the Universe, and an introduction to the math tools needed to discuss the topic, such as the metric system, ratios, or scientific notation. The students are given astrophysical examples of the application of the basic concept, and asked to choose topics they would like to learn more about. They then develop a presentation on this subject, drawing on audio-visual materials at the Observatory, and often making their own drawings to create a poster or oral presentation. They rely heavily on images obtained over the internet and use Mosaic and the Gems of Hubble picture books in much of their research. All the students end the week acquainted with the Observatory computers and the use of the internet to access information.

After spending three or four days preparing, their week culminates in a presentation of their project to their parents, family, and friends at an open night at the Observatory. The children are guides to the Observatory during these nights, and their presentations are extremely well attended. They also present their work to their classmates in school during the following few days and thus become responsible for teaching each other. At the end of the session, those projects that can be displayed easily (posters and viewgraphs) are mounted in the main hallway of the Elementary School. The performance of students is

truly impressive : as an example of densitites, using digital images and Photoshop on our Macintosh, one young girl created an image of a black hole the mass of the earth which just fit inside Nantucket harbor. Another girl created a short hypercard 'movie' which showed a supernova explosion, and delighted in explaining how the center of the star got denser and denser and hotter and hotter until it ran out of fuel and could not hold itself up. Quizzed during a demonstration, she gave even her principal a lesson in stellar astrophysics and computers.

Although this program presently affects few students (typically 20 to 25 in the 4th grade class), as a way to reach the Nantucket community it may be ideal. In this program, the children become the experts, and are responsible for teaching their parents and classmates something really 'neat'. They always succeed. The program involves the parents and brings them into the Observatory, where their children are the guides and the translators of this unknown world of research, computers, and images from space.

With experience we are learning how best to tie the the physics of the Sun and stars to the math curriculum, and find the most effective way to allow other teachers to bring these activities to their classroom. We have plans to expand the program to the other 4th grade classes in the Nantucket Elementary, with help from a recently awarded NASA IDEA grant. Our modest program at Maria Mitchell Observatory may not reach as many students as in larger communities, but it provides a high level of involvement and engagement for children who have few opportunities to see science, to interact with a professional scientist, and to become familiar with technology and computers, in a real research environment (where, by the way, the researchers are college students). If we can offer this experience to all the 4th graders in Nantucket annually, we will gradually reach a very large fraction of the Nantucket community, introduce them to the concepts of scientific research and to notions that expand their perception of the Universe, and acquaint them with technology and exploration beyond their small island world.

7 APPENDIX II. Papers prepared under this grant

Center for Astrophysics
Preprint Series No. 4069
(Received April 4, 1995)

TWO-COMPONENT MODELING OF THE SOLAR IR CO LINES

Eugene H. Avrett
Harvard-Smithsonian Center for Astrophysics

To appear in
Infrared Tools for Solar Astrophysics: What's Next?
Proceedings of the 15th NSO/Sacaramento Peak Workshop

HARVARD COLLEGE OBSERVATORY SMITHSONIAN ASTROPHYSICAL OBSERVATORY
60 Garden Street, Cambridge, Massachusetts 02138

TWO-COMPONENT MODELING OF THE SOLAR IR CO LINES

EUGENE H. AVRETT
Harvard-Smithsonian Center for Astrophysics
60 Garden Street, Cambridge, MA 02138, USA

ABSTRACT

One-dimensional hydrostatic models of quiet and active solar regions can be constructed that generally account for the observed intensities of lines and continua throughout the spectrum, except for the infrared CO lines. There is an apparent conflict between a) observations of the strongest infrared CO lines formed in LTE at low-chromospheric heights but at temperatures much cooler than the average chromospheric values, and b) observations of Ca II, UV, and microwave intensities that originate from the same chromospheric heights but at the much higher temperatures characteristic of the average chromosphere. A model M_{CO} has been constructed which gives a good fit to the full range of mean CO line profiles (averaged over the central area of the solar disk and over time) but this model conflicts with other observations of average quiet regions. A model L_{CO} which is approximately 100 K cooler than M_{CO} combined with a very bright network model F in the proportions $0.6L_{CO}+0.4F$ is found to be generally consistent with the CO, Ca II, UV, and microwave observations. Ayres, Testerman, and Brault found that models COOLC and FLUXT in the proportions 0.925 and 0.075 account for the CO and Ca II lines, but these combined models give an average UV intensity at 140 nm about 20 times larger than observed. The $0.6L_{CO}+0.4F$ result may give a better description of the cool and hot components that produce the space- and time-averaged spectra. Recent observations carried out by Uitenbroek, Noyes, and Rabin with high spatial and temporal resolution indicate that the faintest intensities in the strong CO lines measured at given locations usually become much brighter within 1 to 3 minutes. The cool regions thus seem to be mostly the low-temperature portions of oscillatory waves rather than cool structures that are stationary.

1. Introduction

Because the solar surface can be studied at high spatial resolution, more is known about the atmosphere of the Sun than about any other stellar atmosphere. Even so, the basic structure of the solar atmosphere has not been determined well enough to explain all the available observations.

To a first approximation, a one-dimensional model in hydrostatic equilibrium can be constructed to account for the spectrum emitted from each type of feature seen at high spatial resolution on the solar surface, since the horizontal extent of most features is large compared with the vertical thickness of the emitting region. Thus, different cell and network components of quiet regions, various active regions, sunspot umbrae and penumbrae, and flaring regions can be modeled separately. Suppose the intensity spectrum computed from a one-dimensional model agrees with the observed intensity values from a given component region in lines and continua over a wide range of wavelengths, thus probing a wide range of atmospheric depths. Then we could

conclude that the stratification of temperature and density in the model represents the actual conditions in the observed component region. Such models derived from observed spectra would give useful physical information about the atmosphere, such as the flow of energy in various forms and the heating mechanisms that are most important. However, only rough agreement has been achieved between such models and available observations even when the CO vibration-rotation lines are excluded.

The problem with the CO lines is that 1) they are formed in LTE (Ayres & Wiedemann[1]) so that the observed brightness temperature at each wavelength in a line should be close to the kinetic temperature at unit optical depth for that wavelength, 2) the strongest lines have central brightness temperatures around 4100 K at disk center, and values as small as 3700 K at the solar limb (Noyes & Hall[2]; Ayres & Testerman[3]), whereas 3) all other diagnostics of the solar temperature minimum (e.g., the Ca II and Mg II resonance line wings and the UV and microwave minimum brightness temperature ranges) indicate an average quiet-Sun minimum temperature of at least 4400 K. The CO lines show that part of the atmosphere is much cooler than indicated by these other diagnostics.

In this paper we exhibit a model that fits the average CO spectrum at disk center, and examine how various cool and hot models might be combined to agree with all diagnostics. In Section 4 we call attention to the recent observations of Uitenbroek, Noyes, and Rabin that show the temperature of the cool regions to vary with time.

The results reported here were obtained in collaboration with E. S. Chang, R. L. Kurucz, and R. Loeser. A more complete account is being prepared for publication in The Astrophysical Journal.

2. CO Observations and Modeling

In their Spacelab-3 ATMOS experiment on the Space Shuttle, Farmer & Norton[4] obtained disk-center solar spectra with high spectral resolution throughout the infrared wavelength range λ = 2.1-16.5 μm. They give the intensity averaged over a circular region extending from disk center out to 0.28 solar radii for $\lambda < 4.97$ μm, and out to 0.58 solar radii for $\lambda > 4.97$ μm (2010.5 cm^{-1}). We have selected a set of 215 fundamental and first overtone lines of $^{12}C^{16}O$ and $^{13}C^{16}O$ between 2.3 and 6.9 μm (4350 to 1450 cm^{-1}) for the present study. The set includes very weak lines as well as the strongest ones.

Figure 1 shows the overall results of our CO line calculations based on an atmospheric model M_{CO} adjusted to fit these lines as well as possible. Brightness temperature is plotted as a function of wavenumber. Each of the 215 CO lines in the set is represented by a vertical line extending from the continuum value down to the calculated line-center brightness temperature. There are no CO lines in the gap between the fundamental lines on the left and the first overtone lines on the right. The first overtone lines are formed deep in the photosphere in the temperature range 5700-6300 K, while the fundamental lines have their continuua in the 5300-5700 K range and calculated line centers at brightness temperatures as low as 4200 K.

The solid curve in Figure 2 is the observed CO spectrum near 2239 cm^{-1} (4.466

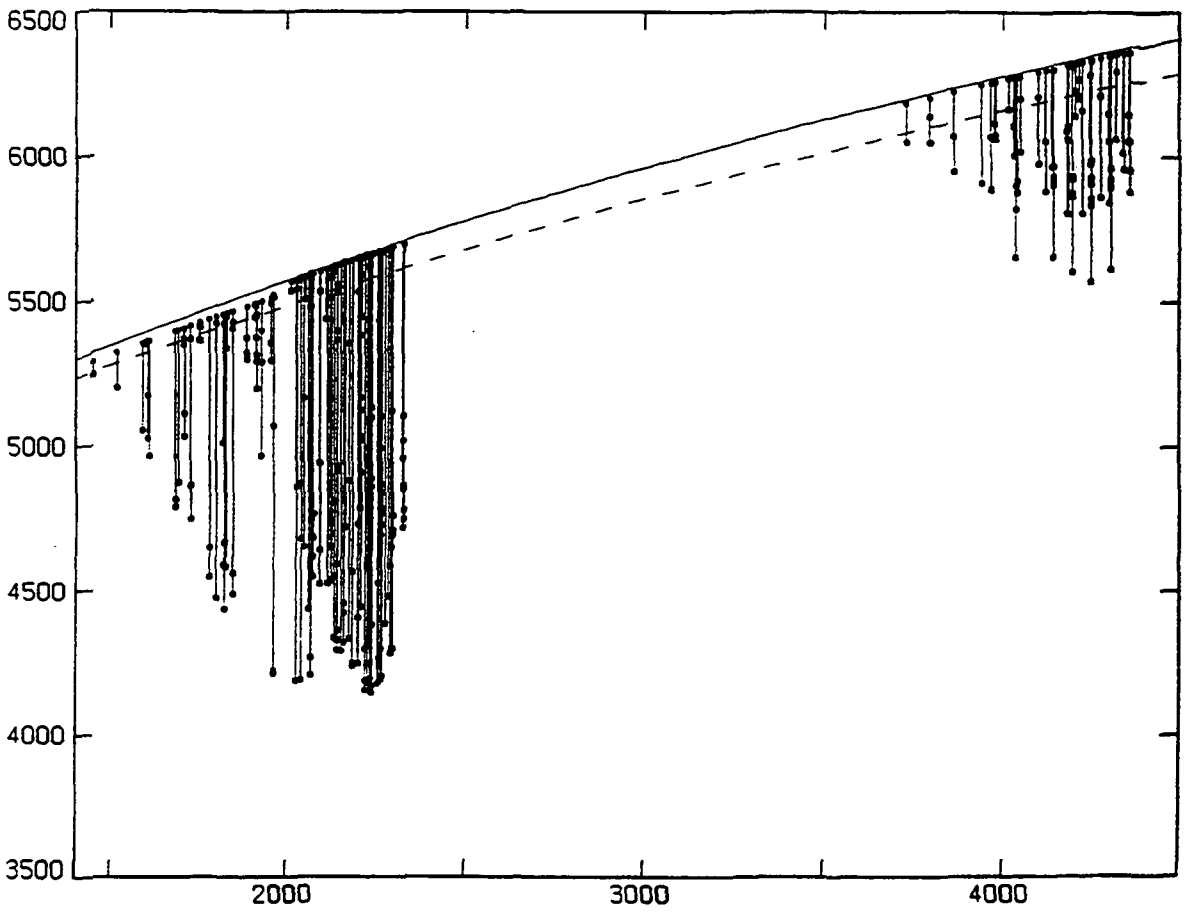

Fig. 1. Calculated brightness temperatures for the 215 CO lines in this study. The solid and dashed lines represent the calculated continuum at disk center and at 0.58 solar radii, respectively.

μm) while the dots represent the spectrum calculated from model M_{CO}. The scale on the left is residual intensity. The corresponding brightness temperature, derived from the calculated continuum, appears on the right. The computed values represent the intensity integrated over the same area of the solar disk as observed. We included the effect of solar rotational broading and attempted to apply the same instrumental broading to the calculated spectrum as in the ATMOS experiment. We used what we considered to be the best available atomic and molecular data and solar abundance values (as will be discussed by Chang, Avrett, Kurucz, and Loeser, in preparation). The temperature distribution was the only function that was adjusted by trial and error in order to get a best fit to the set of CO lines. The corresponding density distribution is determined by assuming hydrostatic equilibrium. The CO lines are assumed to be formed in LTE but the calculated model takes account of non-LTE effects for H^- and the atoms that contribute to the opacity and to the electron density.

Figure 3 shows the temperature as a function of the continuum optical depth at 500 nm for model M_{CO} based on the CO line observations. Each vertical line segment in this figure extends from the central brightness temperature value calculated for a CO line to the observed value for that line, and is thus an approximate measure of the temperature change needed to match the observations. While some further adjustments could be made, the temperature values seem within about 100 K of the best distribution based on these observations. The disk-center CO lines do not give information about temperatures below 4100 K. We have extrapolated model M_{CO} to 3800 K to account for the lower values at the limb, and then introduced a rapid temperature rise to the much higher values in the upper chromosphere.

The temperature distribution in Figure 3 differs substantially from the one that roughly fits other diagnostics of the temperature minimum region and low chromosphere. Figure 4 shows the average quiet-Sun temperature distribution from Maltby et al.[5], and tabulated as model C by Fontenla, Avrett, & Loeser[6]. As before, the vertical line segments indicate the differences between the calculated and observed brightness temperatures in the core of each CO line.

Figure 5 compares the same observed spectrum as in Figure 2 with the one calculted with model C. Since the minimum temperature in the model is 4400 K the calculated values in the cores of the strongest lines cannot be any smaller. Note that there are also some systematic differences between the two models in the deeper layers.

3. Comparisons With UV Data

Now consider the observed and calculated intensities in the UV wavelength range 135-174 nm. The dots and crosses in Figure 6 are observations of the disk-center continuum intensity (between various emission and absorption lines) by Brekke[7] and Samain[8], respectively. The dashed lines indicate the brightness temperatures that correspond to the intensity at a given wavelength. Brekke & Kjeldseth-Moe[9] report that recent UV observations with a better absolute calibration than before imply that the minimum observed brightness temperature at disk center should be increased

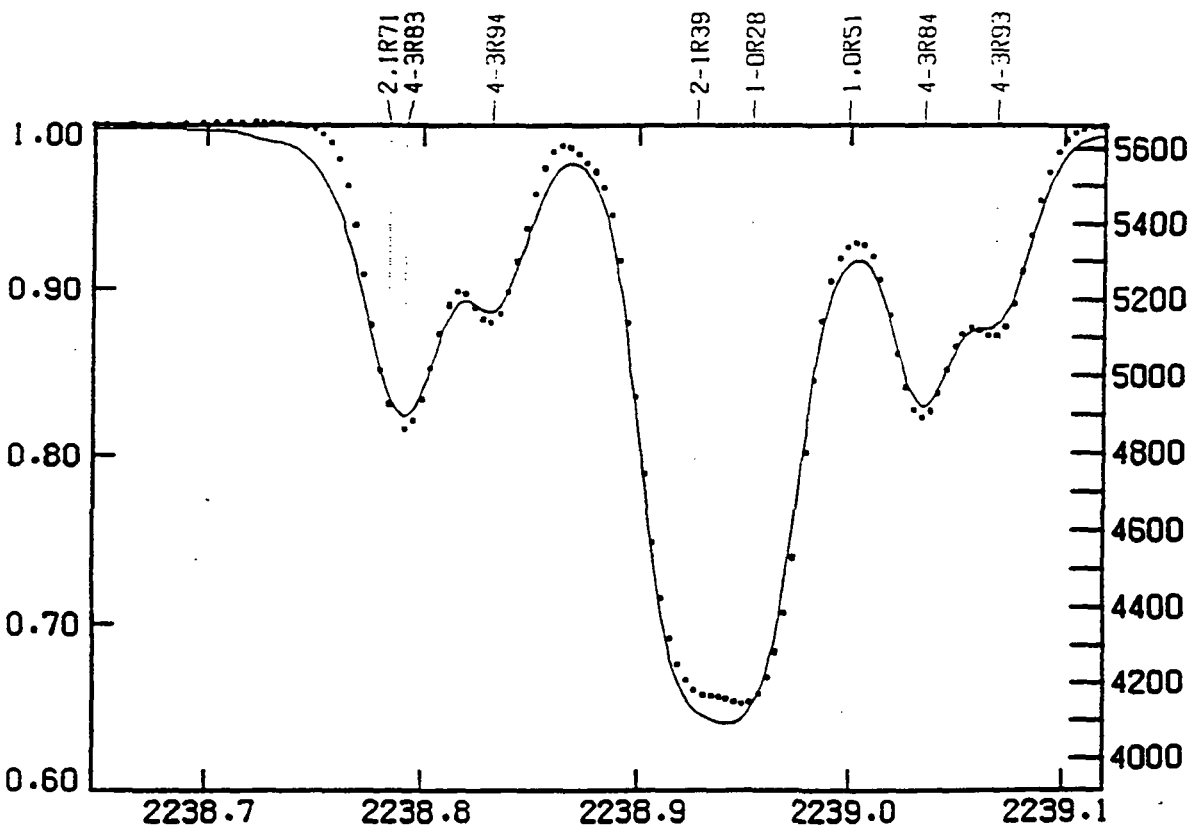

Fig. 2. CO spectrum near 2239 cm^{-1} (4.466 μm) from model M_{CO} (dots) compared with the ATMOS observations of Farmer and Norton (solid line). The scale on the left is residual intensity. The corresponding brightness temperatures appear on the right. Hyphens are used in the CO line designations at the top for $^{12}C^{16}O$, and commas for $^{13}C^{16}O$.

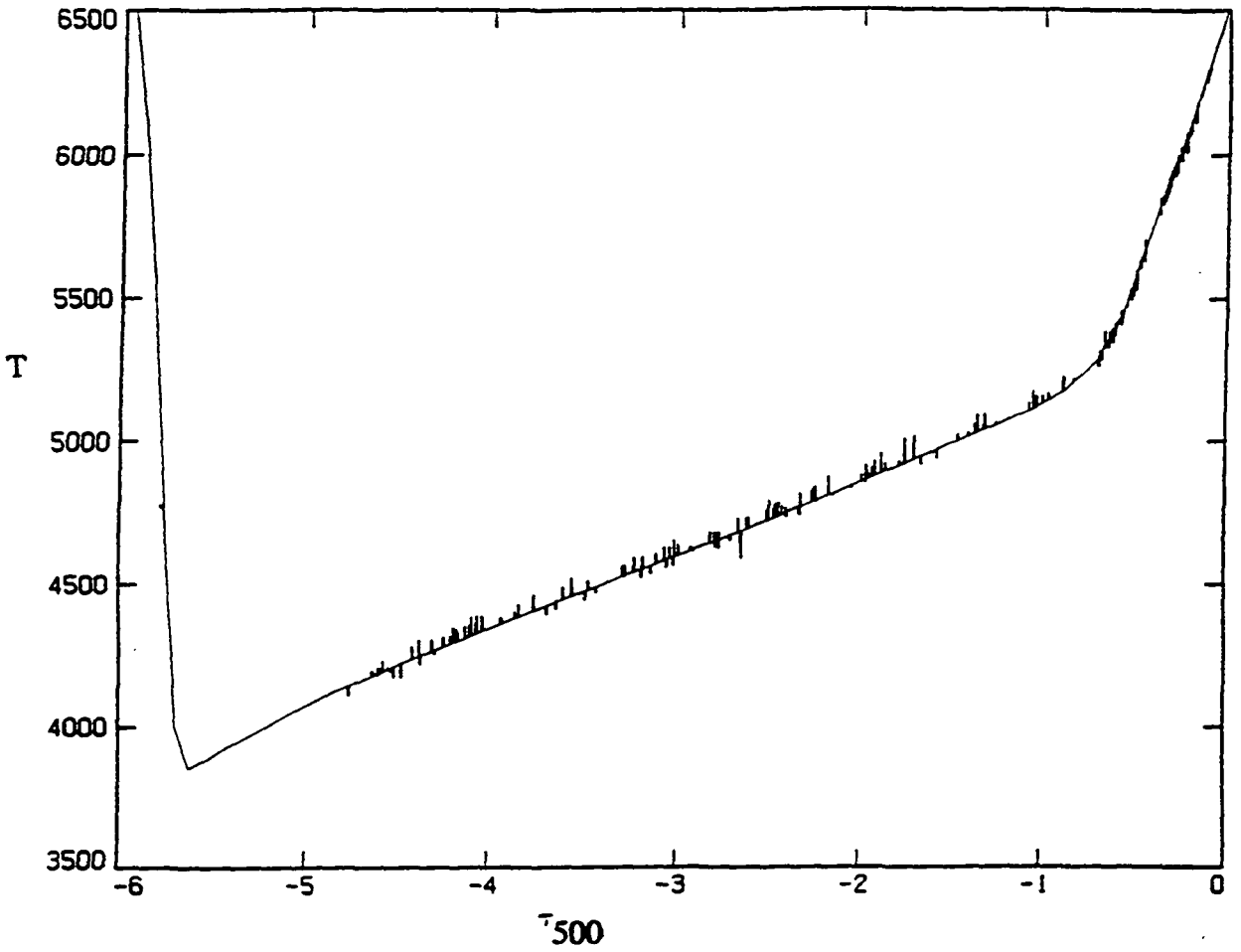

Fig. 3. T vs. τ_{500} for model M_{CO}. The vertical line segments indicate the differences between the calculated and observed brightness temperatures in the core of each CO line.

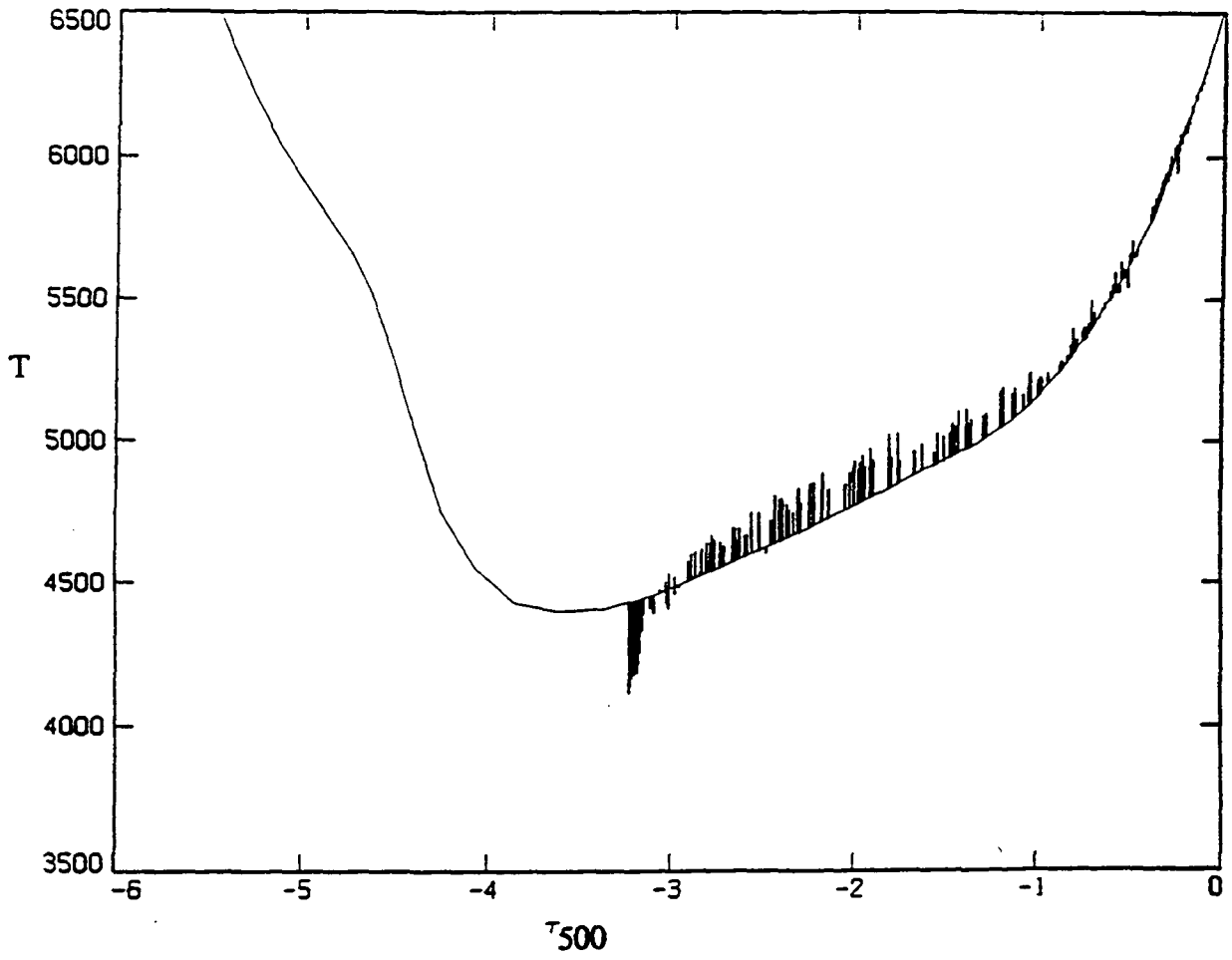

Fig. 4. T vs. τ_{500} for model C. The vertical line segments have the same meaning as in Figure 3.

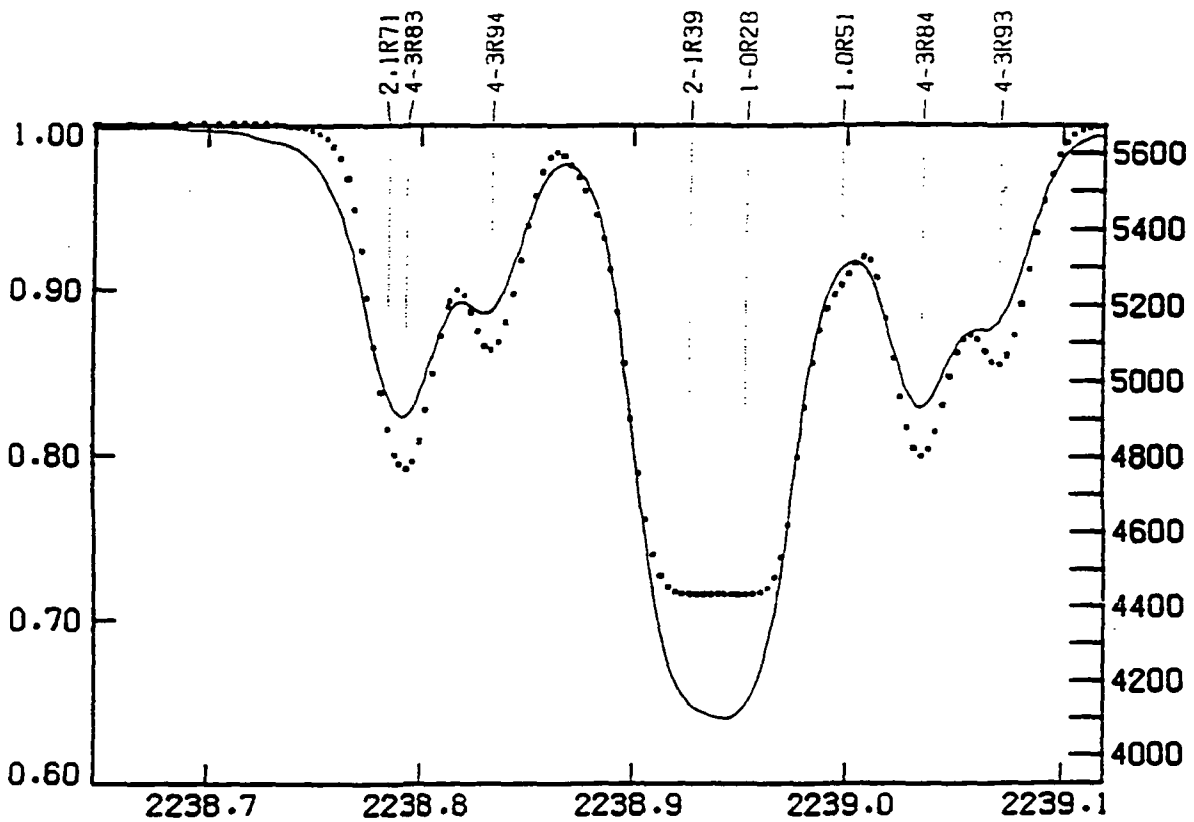

Fig. 5. Same as Figure 2 except that the calculated values are from model C.

from 4450±50 K to 4520±25 K. (This upward adjustment has not been applied to the observations in Figure 6.)

The curves labeled C and M_{CO} are the intensity distributions that are calculated from these two models. These are non-LTE calculations that include the overall effects of absorption and emission lines in the spectrum. Note that the model C intensities are in reasonable agreement with the observations while the model M_{CO} intensities are too low by a factor of 2 or more. We also plot the intensity distributions calculated from the COOLC and FLUXT models of Ayres, Testerman, & Brault[10]. They found that these separate cool and hot models when combined together with relative covering factors 0.925 and 0.075, respectively, approximately account for both the infrared CO line observations and the emission observed in the Ca II K line. However, the intensity at 140 nm from this combination of COOLC and FLUXT models is about 20 times larger than observed.

What other combination of cool and hot models might explain not only the CO and Ca II lines but also these UV observations? We have found that a model L_{CO}, roughly 100 K cooler than M_{CO}, combined with the very bright network model F given by Fontenla, Avrett, & Loeser[6], with relative covering factors 0.6 and 0.4 is consistent with the CO, Ca II, and UV observations. The UV results are shown in Figure 7. This combination is also consistent with observations in the far-infrared and sub-millimeter range where the emission also originates in the temperature minimum region and low chromosphere.

4. Discussion

Observations of the infrared CO lines indicate the presence of a cool component in the atmosphere at low-chromospheric heights. The CO lines are highly sensitive to this cool component because of the rapid increase of the CO line opacity with decreasing temperature in the 3500-4500 K range. Other diagnostics are not as sensitive to these low temperatures, and do not require the two-component modeling discussed above. However, our $0.6L_{CO}+ 0.4F$ combined model seems to explain both the CO observations and the other diagnostics.

The contrast in Figure 7 that might be resolved at very high spatial resolution is greater than that observed by Foing & Bonnet[11]. Their spatial resolution was sufficient to detect any features of 1-2 arc sec size. They found the maximum brightness temperature between the bright network and the darkest internetwork features to be roughly 150 K at 160 nm. This may indicate that model F is too bright to serve as the hot component in this simple modeling procedure, or that we must consider the radiative interaction between the component regions in calculating the spectrum.

Another interpretation is that the two components are not spatially distinct and constant with time, but that local time variations are important. This view is strongly supported by recent observations by Uitenbroek, Noyes, & Rabin[12] and Uitenbroek & Noyes[13] who obtained spatially and temporally resolved CO spectra near 4.67 μm with a new infrared array detector at the McMath-Pierce solar telescope at Kitt Peak. Fig. 2 of Uitenbroek & Noyes shows a space-time map of the 3-2 R14 line-

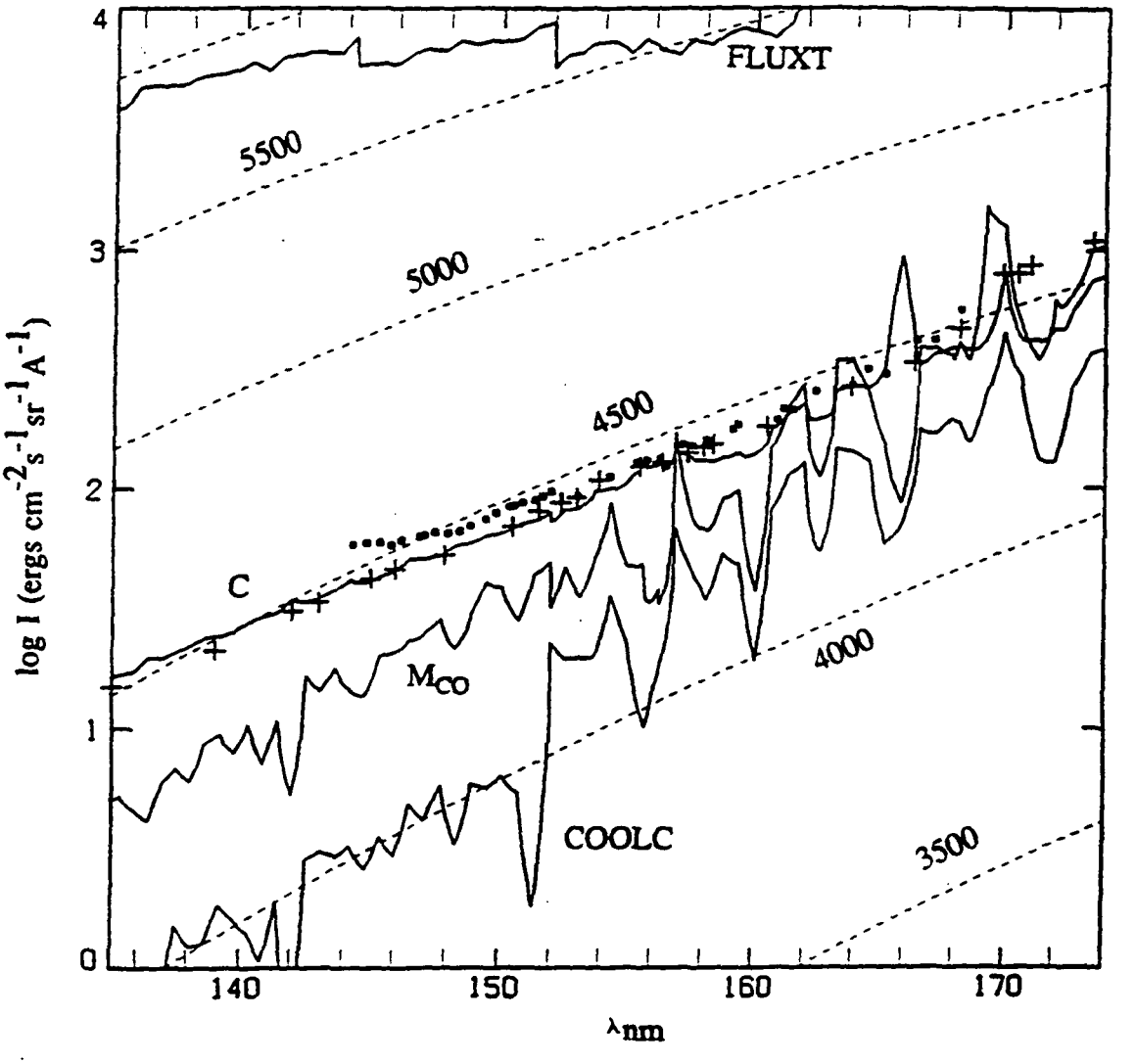

Fig. 6. Observed and calculated disk-center intensities in the UV wavelength range 135-174 nm. Brightness temperatures are indicated by dashed lines. The dots and crosses are continuum observations by Brekke and Samain, respectively. The calculated distributions include sampled opacities due to various lines. Calculated results are shown for models COOLC, M_{CO}, C, and FLUXT.

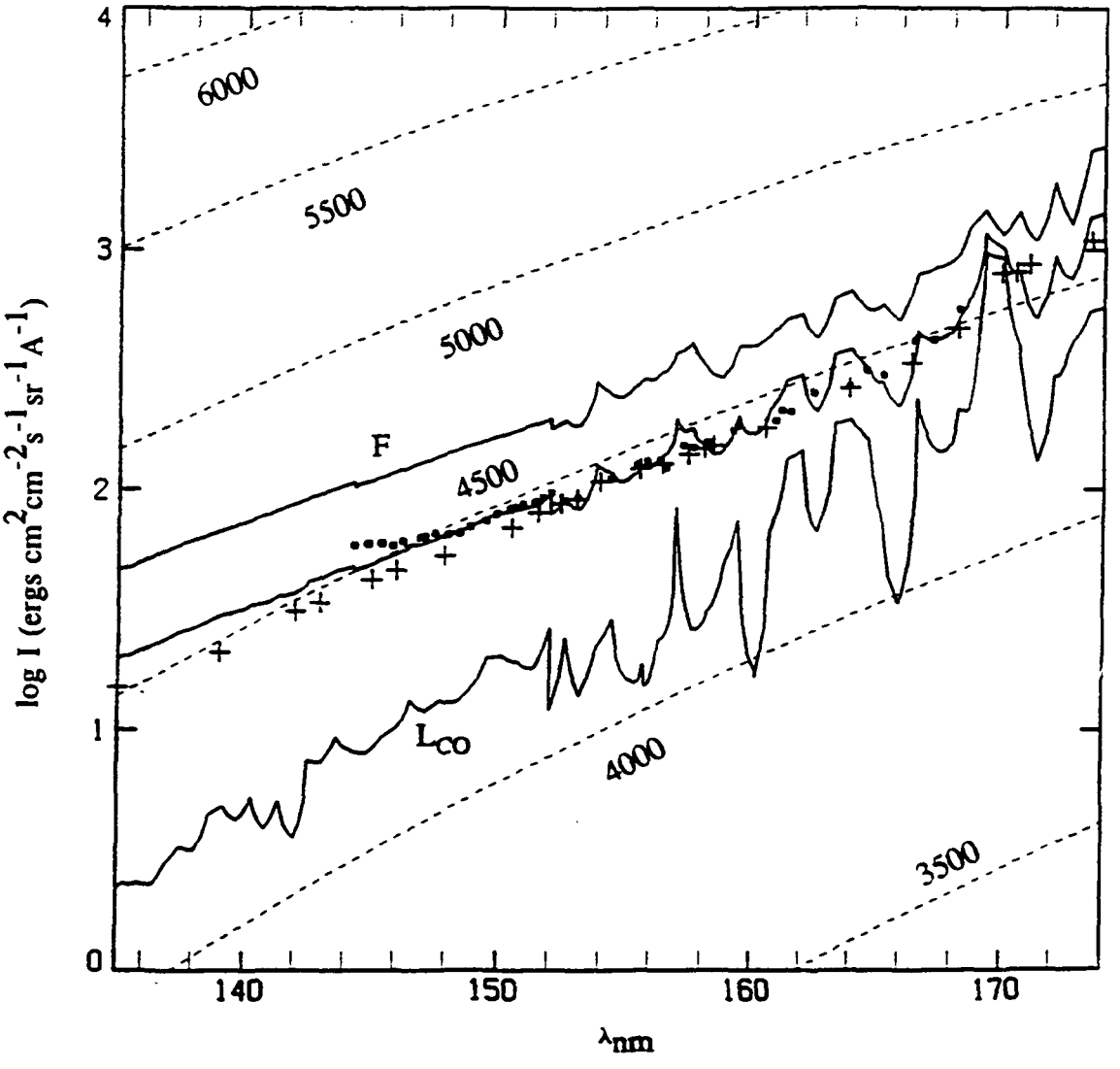

Fig. 7. Same as Figure 6 except that the lower and upper calculated intensities are from models L_{CO} and F, and the middle distribution represents $0.6L_{CO}+0.4F$.

core brightness temperature along a 94 arcsec slit placed over a quiet region near disk center during a period of 23 minutes. They find peak-to-peak temperature fluctuations of approximately 400 K and substantial time variations at each position. These observations clearly show that dynamical effects play an important role in determining the low temperatures seen in the cores of the strong CO lines.

5. Acknowledgements

This research was supported by NASA Grants NAGW-3299 and NAGW-2545.

6. References

1. T. R. Ayres and G. R. Wiedemann, *ApJ,* **338** (1989) 1033.
2. R. W. Noyes and D. N. B. Hall, *ApJ,* **176** (1972) L89.
3. T. R. Ayres and L. Testerman, *ApJ,* **245** (1981) 1124.
4. C. B. Farmer and R. H. Norton, *A High-Resolution Atlas of the Infrared Spectrum of the Sun and the Earth Atmosphere from Space*, NASA Pub. 1224, 1989, vol. 1.
5. P. Maltby, E. H. Avrett, M. Carlsson, O. Kjeldseth-Moe, R. L. Kurucz, and R. Loeser, *ApJ,* **306** (1986) 284.
6. J. M. Fontenla, E. H. Avrett, and R. Loeser, *ApJ,* **406** (1993) 319.
7. P. O. L. Brekke, *Observed Structure and Dynamics of the Solar Chromosphere and Transition Region Based on High Resolution Ultraviolet Spectrograms*, Ph.D. Thesis, University of Oslo, 1992.
8. D. Samain, *A&A,* **74** (1979) 225.
9. P. O. L. Brekke and O. Kjeldseth-Moe, *ApJ,* **431** (1994) L55.
10. T. R. Ayres, L. Testerman, and J. W. Brault, *ApJ,* **304** (1986) 542.
11. B. Foing and R. M. Bonnet, *A&A* **136** (1984) 133.
12. H. Uitenbroek, R. W. Noyes, and D. Rabin, *ApJ,* **432** (1994) L67.
13. H. Uitenbroek and R. W. Noyes, *Chromospheric Dynamics*, ed. M. Carlsson (Institute of Theoretical Astrophysics, University of Oslo, Norway, 1994), p. 129.

THE ASTROPHYSICAL JOURNAL, 432:L67–L70, 1994 September 1

IMAGING SPECTROSCOPY OF THE SOLAR CO LINES AT 4.67 MICRONS

HAN UITENBROEK AND R. W. NOYES
Harvard-Smithsonian Center for Astrophysics, 60 Garden Street, Cambridge, MA 02138
AND
DOUGLAS RABIN
National Solar Observatory, National Optical Astronomy Observatories,[1] P.O. Box 26732, Tucson, AZ 85726
Received 1994 March 23; accepted 1994 May 26

ABSTRACT

We analyze spatially and temporally resolved spectra of the fundamental vibration-rotation transitions of carbon monoxide (CO) in the solar spectrum at 4.67 μm. Our observations imply that, in the quiet Sun, spatial variations in CO intensity are largely dynamical in nature, reinforcing the suggestion that dynamical effects play a key role in the formation of the dark CO cores. Time sequences of resolved spectra exhibit mainly 3 minute power in line-core intensity but mainly a 5 minute period in Doppler shift. The weak 7–6 R68 line shows normal Evershed flow in the penumbra of a sunspot; we find evidence for the onset of inverse Evershed flow in the strong 3–2 R14 line. Spectra at the limb indicate that 3–2 R14 emission extends approximately 360 km beyond the continuum limb.

Subject headings: infrared: general — line: formation — Sun: atmosphere — Sun: ocillations

1. INTRODUCTION

The vibration-rotation lines of carbon monoxide (CO) have been enigmatic ever since observations at the solar limb by Noyes & Hall (1972a), and later Ayres & Testerman (1981), indicated the presence of gas as cool as 3700 K. Non-LTE atmospheric models predict that the CO lines form in LTE in the temperature-minimum region, where they should accurately reflect electron temperature (Ayres & Wiedemann 1989). This makes them especially valuable diagnostics of the thermal stratification in the atmosphere of the Sun and other cool stars. However, no other spectral diagnostic, except perhaps the strong rotational lines of the OH radical (Deming et al. 1984), has as yet confirmed the low CO temperatures at the limb. Rather, they differ markedly from the higher values ($\sim$4400 K) derived from "hot" diagnostics such as the broad wings of the Ca II H and K and Mg II *h* and *k* lines (Ayres & Linsky 1976; Maltby et al. 1986). These disparate diagnostics may be reconciled by positing that hot spatial inhomogeneities, associated with concentrated magnetic fields, are immersed in a cooler ambient atmosphere (Ayres, Testerman, & Brault 1986). On the other hand, observations suggest that a significant fraction of the cool gas may have a dynamical origin, due to the decompression phase of nearly adiabatic oscillations. Noyes & Hall (1972b) and Ayres & Brault (1990) found temperature fluctuations with peak-to-peak amplitudes of 225–300 K and a clear 5 minute period in the cores of strong CO lines. In addition, numerical simulations of granulation (e.g., Malagoli, Cattaneo, & Brummel 1990) indicate substantial cooling above the center of upwelling granules; such effects could also contribute to the low temperatures observed in CO lines.

It has been suggested (Ayres 1981; Kneer 1983; Muchmore & Ulmschneider 1985) that radiative cooling by the CO molecule itself is responsible for the thermal bifurcation, in that a local decrease in temperature allows more molecules to form and thereby increases the radiative losses. Anderson (1989) and Mauas, Avrett, & Loeser (1990) found no evidence for such an instability in numerical calculations that took detailed account of the multitude of CO lines and the CO dissociation equilibrium. However, Anderson & Athay (1989) suggested that the thermal structure of the atmosphere critically depends on the amount of mechanical heat input in the region where CO cooling begins, just above the classical temperature minimum. Local variations in mechanical energy dissipation in that region—due, for example, to the presence of concentrated magnetic fields or hydrodynamic shocks—might produce a bifurcated atmosphere.

This brief synopsis of contending hypotheses shows that observations of spatiotemporal variations of the CO lines are key to understanding the origin of very cool material in the temperature-minimum region. Earlier observations with single-element infrared detectors (which are impractical for building up a two-dimensional spatial image) were hampered by low spatial resolution, which may lead to an underestimate of actual temperature fluctuations if these occur on small spatial scales. In this paper we take advantage for the first time of the imaging capabilities of an array detector at 4.67 μm, to address the relative importance of spatial inhomogeneities and temporal fluctuations in producing the observed CO behavior.

2. OBSERVATIONAL PARAMETERS AND DATA REDUCTION

We used the infrared grating of the 13.8 m vertical spectrograph on the 1.5 m main telescope of the NSO McMath-Pierce facility on Kitt Peak to obtain high-resolution ($\nu/\Delta\nu \approx 90{,}000$) spectra of the CO lines in the atmospheric window around 2143 cm^{-1} (4.67 μm). A narrow-band filter was used to isolate the second order, for which the theoretical diffraction-limited resolving power is 110,000. Spectra were recorded with a 256 × 256 InSb array camera (Amber Engineering) behind minifying transfer optics. This setup imaged a 2.5 cm^{-1} portion of the spectrum on the detector. The 250 μm–wide slit subtended an area of 0.″63 × 51″ on the Sun. The detector provided a spatial sampling of 0.″2 pixel^{-1} along the slit; since

[1] Operated by the Association of Universities for Research in Astronomy (AURA), Inc., under cooperative agreement with the National Science Foundation.

the diffraction-limited resolution of the telescope is 0".77 at 4.67 μm, this oversamples the spectrum perpendicular to the dispersion. We subtracted dark frames obtained by exposing with the spectrograph slit closed, and then divided the results by appropriate flat-field images. The flat fields were obtained for each sequence by moving the telescope over the solar surface during exposure and averaging 8–12 frames, and then removing the spatially averaged spectrum by averaging each column of the array (along the slit) and dividing each pixel (spatial location) in that column by the average. Finally, we removed bad pixels from the dark-subtracted and flat-fielded frames by interpolation from neighboring pixels at the same wavelength.

We operated the instrument in two modes, with different trade-offs between spatial and temporal resolution. In one mode we scanned the solar image over the slit to build spectra-spectroheliograms, data cubes that contain a spectrum for each spatial pixel covered by the scan. From the data cube we can construct a two-dimensional image of any function of the spectral distribution, such as the Doppler shift or intensity in the core of a line. This mode is presently limited by the throughput of the data system: although the camera could record data faster (at 27 Hz), reading out the digital data and writing it to disk takes almost 5 s. Thus, only a small area can be scanned before surface features evolve. We therefore employed a second mode—time-sequence spectra—in which the slit is kept at a fixed position; this exchanges the second spatial dimension for much better temporal resolution.

From the spectra-spectroheliograms and time-sequence spectra we constructed maps (space-space and space-time, respectively) of the core intensity and frequency shift of various lines. We made parabolic fits to the lowest three points of each line profile and determined the position of the minimum of the fitted profile. Doppler shifts are specified with respect to the average position of the line, with blueshift (corresponding to upward mass motions) coded light and redshift coded dark. Because the CO lines form in LTE, relative intensities map directly into temperature variations. To fix temperatures on an absolute scale, we assumed that the average intensity over the scan corresponded to an average brightness temperature estimated from the ATMOS atlas of the solar infrared spectrum (Farmer & Norton 1989), with the observed continuum level matched to the theoretical value predicted by model C of Fontenla, Avrett, & Loeser (1993) for the average quiet Sun. The use of the minimum value of the parabolic fit to the line, rather than the intensity at a fixed wavelength, decouples the determination of brightness temperature fluctuations from the velocity signal.

3. THE QUIET SUN

3.1. *Spectra-Spectroheliograms*

The top half of Figure 1 (Plate L4) presents maps of a 50" × 50" quiet area at disk center obtained on 1993 October 5. The top two rows show the variations of brightness temperature (*left-hand panels*) and Doppler shift (*right-hand panels*) in a weak line (7–6 R68) and a strong line (3–2 R14). Table 1 lists average brightness temperatures of these two lines and an intermediate-strength line, together with their rms temperature and Doppler shift variations. The weak-line temperature map appears predominantly dark, with isolated bright points of 3"–4" size and somewhat less bright areas of larger extent which appear fuzzier. Blinking between frames in different lines (7–6 R68; 6–5 R47, which is not shown here; and 3–2 R14) reveals a common pattern with a shape and size similar to the familiar chromospheric network; we tentatively associate the pattern with that magnetic network. However, the "network" pattern is much less prominent in the 3–2 R14 line (Fig. 1, *second-row panels*); this suggests that magnetic effects play a relatively less important role than dynamical effects at this higher level of formation. The amplitudes of variations increase with formation height, and their distribution becomes slightly skewed to lower temperatures by small-area cold elements that are as much as 200 K colder than the average. The bulk of the 3–2 R14 temperature variations, however, remains within ± 100 K, as shown in Table 1.

TABLE 1

BRIGHTNESS TEMPERATURES AND rms TEMPERATURE AND LINE-SHIFT VARIATIONS

CO Line	T_b (K)	rms(ΔT) (K)	rms(Δv) (km s^{-1})
3–2 R14.....	4366	91	0.37
6–5 R47.....	4679	58	0.28
7–6 R68.....	5030	40	0.28

Both Doppler maps (*right-hand panels*) show the typical patchiness of the 5 minute oscillations with larger spatial scales than the temperature maps. There is no obvious correlation between the intensity and (simultaneous) line-shift maps, nor is there clear evidence of the network elements in the latter. A granulation pattern is not recognizable in either of the two lines, or in a map of the continuum (not shown here); however, this could be a consequence of seeing, which was typically no better than 1".5. Indeed, in a quiet-Sun spectra-spectroheliogram taken at $\mu = 0.5$ in more favorable seeing, we observe hints of the granulation pattern, which appears as a set of bright rings with dark centers. This observation suggests the need for further investigation into the effect of granular overshoot and adiabatic expansion as another possible cause of the observed low CO temperatures. A similar suggestion has been made by Solanki, Livingston, & Ayres (1994).

3.2. *Time-Sequence Spectra*

We studied the temporal behavior of the CO lines to probe the thermal response of the upper atmosphere to the velocity field induced by the global 5 minute oscillations. On 1993 October 9 we obtained a sequence of 240 slit spectra with the array camera. The slit was kept fixed over a quiet region on the center of the disk while spectra were taken at a rate of 8.6 s per frame. The bottom two rows of Figure 1 show space-time diagrams of the evolution of temperature (*left-hand panels*) and Doppler shift (*right-hand panels*) of the weaker 7–6 R68 line and the stronger 3–2 R14 line, respectively. In both lines, the temporal pattern of the brightness differs from that of the Doppler shift: clear 5 minute power in Doppler shift compared with more frequent and less regular fluctuations in temperature. Figure 2 shows temporal power spectra, averaged over the length of the slit, of Doppler shift for 3–2 R14 and intensity variation for 3–2 R14 and 7–6 R68. The curves are in agreement with observations by Deming et al. (1986), who found predominantly 5 minute oscillations (3.3 mHz) in Doppler shift of a strong OH line at 903.8 cm^{-1}, but higher frequency (4.3 mHz) oscillations in intensity. The apparent spatial scale of the Doppler-shift fluctuations is typical of 5 minute oscillations (e.g., Musman & Rust 1970); the spatial scale of the temperature fluctuations is noticeably smaller.

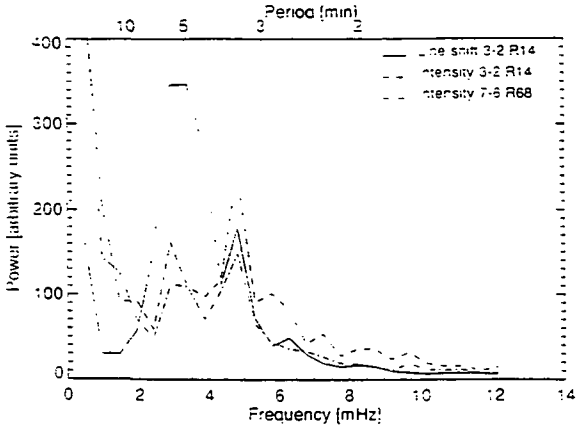

FIG. 2.—Power spectra of fluctuations of temperature (*solid line*) and line shift (*dashed line*) in the strong 3–2 R14 line and intensity of the weaker 7–6 R68 line (*dot-dash line*) from the quiet-Sun time sequence displayed in the bottom two rows of Fig. 1. Power was averaged over the length of the slit.

Thus, the core intensity and shift of the emergent profile are modulated differently, reflecting different weighted averages over the same (wavelength-dependent) contribution function. It is well known that the amplitude of 3 minute relative to 5 minute oscillations increases with altitude in the atmosphere (e.g., Fleck & Schmitz 1991; Kalkofen et al. 1994). Also, the ratio of amplitudes of thermal and velocity oscillation increases with increasing altitude; this is because deep in the atmosphere, radiative relaxation times are short and temperature perturbations are quickly damped by photon losses, while at higher altitudes slower relaxation leads to a more nearly adiabatic response to 3 minute or 5 minute oscillations (Noyes & Leighton 1963). Because of the weak temperature response of the deeper layers, the oscillation field modulates mainly the high-altitude tail of the brightness contribution function and hence the core of the line profile. Velocity excursions, on the other hand, occur over the entire range of the contribution function, thus modulating the entire emergent profile. The differential behavior of line intensity and shift should provide a useful constraint on models of CO line formation.

Both temperature maps (*left-hand panels*) show a bright, steadily emitting feature that drifts toward the left of the diagram with time, which we identify with a network element. The drift is due to telescope tracking errors rather than movement on the Sun. Although this feature consitutes the brightest element in the 7–6 R68 intensity map, this is not the case for the 3–2 R14 line. Notice that the drifting element cannot be discerned in the space-time Doppler maps (*right-hand panels*). This reinforces our earlier conclusion that the magnetic network is not imprinted in the pattern of the spatial Doppler maps. Overall, the time series confirms the picture suggested by the spatial maps in the previous section: in the higher-lying 3–2 R14 line the magnetic network is less conspicuous than in the weaker line, and the temperature variations (both positive and negative) in the former seem to be dominated by dynamical phenomena. Finally, the time-sequence spectra show a correlation between temperature and Doppler shift, which is largest for a time delay of slightly less than 1 minute, with maximum redshift leading maximum temperature.

4. ACTIVE REGION

The top panel in Figure 3 (Plate L5) shows temperature variations in the core of 7–6 R68 in a complex sunspot (active region NOAA 7592, observed on 1993 October 5 at heliographic position S14 E13). The slit was oriented north-south (heliographic), with north (disk center direction) toward the top. The strong-line map (not shown here) is different in several respects. The area just outside the penumbra appears brighter in the weak line, whereas the two dark pores to the right appear bright in the strong-line image. The second panel from the top in Figure 3 shows the simultaneous map of Doppler shifts. Immediately evident is the Evershed flow, which is sharply confined to the infrared penumbra with outwardly directed flows of ~ 1 km s^{-1} (line-of-sight component) appearing as redshift on the limbward wide (*bottom*) and blueshift toward disk center. Given the small inclination of the local vertical to the line of sight, the horizontal Evershed flow must be substantially larger. The flow is less pronounced in the stronger 3–2 R14 line (not shown here; however, see below). Note the small, isolated areas of flow near the middle of the map; they have no visible counterparts in the intensity map.

The third panel in Figure 3 displays a space-time map of the line shift in the 3–2 R14 line from the same active region observed 3 days later at coordinates S16 W41. The slit was positioned over one of the umbrae and again oriented north-south, with the top of the image toward disk center. The simultaneous continuum map shows the umbra to occupy the region between 20″ and 32″ on the vertical image scale. The Dopplergram exhibits two striking features. First, in addition to the normal photospheric Evershed (out)flow, there also appear velocities of opposite sense (i.e., blueshift on the limbward side and redshift toward disk center). This may reveal the onset of the "inverse" Evershed flow that is observed in chromospheric lines like Hα (Moore & Rabin 1985), and in the 12 micron Mg I lines (Deming et al. 1988). Second, there are clear 5 minute velocity oscillations in the umbra. They appear to propagate outward, resulting in a sequence of horizontal V-shapes in the space-time diagram. The temporal power spectra of 3–2 R14 line shift and intensity in this umbra show distinct peaks at both 3 and 5 minutes. Umbral oscillations of 3 and 5 minutes have been observed before in photospheric lines that form around the temperature-minimum region (e.g., Lites & Thomas 1985). Chromospheric and transition region lines predominantly show 3 minute power (see the reviews by Moore & Rabin 1985 and Thomas 1985).

5. LIMB SPECTRUM

We are especially interested in the behavior of the CO lines at the limb, where they provide a view of the stratification of the atmosphere that is less model-dependent than at disk center. Recently, Solanki et al. (1994) employed a sequence of point spectra stepping across the limb to infer that the solar atmosphere may be described by three components: one hot and two cold ($T \approx 3000$ K) components, one of which should have a chromospheric temperature rise starting higher than 1000 km. However, it is difficult to estimate the accuracy of the radial positions at which the spectra used by Solanki et al. were taken, as they were necessarily obtained at different times in a condition of varying seeing. However, any model using limb spectra depends critically on an accurate knowledge of the relative heights of observation, since spectral intensities drop very rapidly above the continuum limb. Therefore, it is preferable to analyze data such as those presented here, where the use of array detector technology allows spectra to be obtained for all radial positions simultaneously and with accurate coregistration. A model atmosphere analysis of the present data

will be provided in a subsequent paper; here we exhibit the data and make some general comments.

The bottom panel in Figure 3 shows a limb spectrum from a series of 14 obtained near the east limb on 1993 October 5. To improve sampling in the radial direction, we oriented the slit at an angle of 21°.5 to the limb tangent. We selected four of the frames with best seeing by looking for the presence of small-scale variations in the line shape on the disk. The single spectrum reproduced in Figure 3 shows several of these small-scale variations, which appear as "knots" in the absorption lines and represent areas of substantial line broadening. We spatially aligned the four selected frames and determined the intensity profiles (averaged over the frames) at selected wavelengths: the continuum between 2–1 R6 and 3–2 R14, the strong 3–2 R14 line, and the weaker 7–6 R68 line. In Figure 4 we plot the limb profiles of intensity relative to disk-center continuum intensity as a function of radial distance across the limb (which is chosen arbitrarily to fall halfway on the steep slope of the drop-off in continuum intensity). The figure shows that the lines go into emission over the limb and that 3–2 R14 intensity extends approximately 0".5 (360 km) beyond the continuum limb. The error bars on the strong-line profile represent 1 standard deviation from the mean over the four best frames. They provide an estimate of the uncertainty with which the difference in formation height can be established, including local variations in the atmosphere. Our limb profiles differ from those of Solanki et al. (1994; their Fig. 2) in the relative behavior of the 3–2 R14 line and the continuum; this difference needs further investigation.

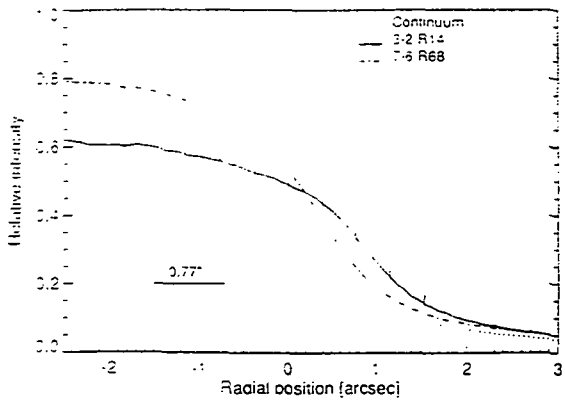

FIG. 4.—Limb profile of the intensity in the continuum (*solid line*), a weak line (*dot-dash line*), and a strong line (*dashed line*). The slit was oriented at an angle of 21°.5 to the limb tangent to give finer sampling perpendicular to the limb.

6. CONCLUSION

We have presented exploratory observations of the CO fundamental vibration-rotation lines at 4.67 μm, using for the first time the imaging capabilities of an array detector at that wavelength. Because the CO lines form in LTE, such observations can clearly probe the spatial structure and temporal behavior of the temperature-minimum region. In quiet areas, bright isolated network elements seem to dominate the thermal structure at the height of formation of 7–6 R68. Higher up, the stronger 3–2 R14 line shows a different topology, with thermal structure dominated by hydrodynamic perturbations that occasionally give rise to isolated low-temperature spots (200–300 K below average). It is at these higher altitudes, which are best probed close to the limb, that the discrepancy between CO line-core and Ca II and Mg II diagnostics appears. The gradual transition to a dynamically dominated atmosphere with increasing altitude suggests that hydrodynamic perturbations may indeed play a key role in the temperature dichotomy. In a future paper we will study spatial and space-time maps at different μ-values, comparing them with simultaneous Ca K-line images.

We observe that the spatial scale of the intensity (predominantly 3 minute) oscillations is somewhat smaller than that of the velocity (predominantly 5 minute) oscillations. This might explain why, with limited spatial resolution, Noyes & Hall (1972b) and Ayres & Brault (1990) found little intensity power at 3 minutes compared with 5 minutes. Use of the array detector permits improved resolution and shows the presence of higher amplitude temperature variations with substantially more power at 3 minutes. This constrains models of CO line formation to those in which the lines form high enough in the atmosphere so that their contribution functions sample the 3 minute oscillations.

The low temperatures in sunspot umbrae and penumbrae selectively strengthened the CO lines, making them well suited to study systematic motions. The onset of the inverse Evershed effect that is observed in the 3–2 R14 line deserves particular attention because it bridges the gap between photospheric lines and chromospheric lines like Hα.

We thank D. B. Jaksha and C. Plymate for supporting the observations and contributing to the development of the infrared camera. We thank the referee, Drake Deming, for useful comments. This work was made possible in part by NASA grant NAGW-2545.

REFERENCES

Anderson, L. S. 1989, ApJ, 339, 558
Anderson, L. S., & Athay, R. G. 1989, ApJ, 336, 1089
Ayres, T. R. 1981, ApJ, 244, 1064
Ayres, T. R., & Brault, J. W. 1990, ApJ, 363, 705
Ayres, T. R., & Linsky, J. L. 1976, ApJ, 205, 874
Ayres, T. R., & Testerman, L. 1981, ApJ, 245, 1124
Ayres, T. R., Testerman, L., & Brault, J. W. 1986, ApJ, 304, 542
Ayres, T. R., & Wiedemann, G. R. 1989, ApJ, 338, 1033
Deming, D., Boyle, R. J., Jennings, D. E., & Wiedemann, G. 1988, ApJ, 333, 978
Deming, D., Glenar, D. A., Käufl, H. U., Hill, A. A., & Espenak, F. 1986, Nature, 322, 232
Deming, D., Hillman, J. J., Kostiuk, T., Mumma, M. J., & Zipoy, D. M. 1984, Sol. Phys., 94, 57
Farmer, C. B., & Norton, R. H. 1989, A High-Resolution Atlas of the Infrared Spectrum of the Sun and the Earth Atmosphere from Space (NASA Ref. Publ. 1224, Vol. 1)
Fieck, B., & Schmitz, F. 1991, A&A, 250, 235
Fontenla, J. M., Avrett, E. H., & Loeser, R. 1993, ApJ, 406, 319
Kalkofen, W., Rossi, P., Bodo, G., & Massaglia, S. 1994, A&A, 284, 976
Kneer, F. 1983, A&A, 128, 311
Lites, B. W., & Thomas, J. H. 1985, ApJ, 294, 682
Malagoli, A., Cattaneo, F., & Brummel, N. H. 1990, ApJ, 361, L33
Maltby, P., Avrett, E. H., Carlsson, M., Kjeldseth-Moe, O., Kurucz, R. L., & Loeser, R. 1986, ApJ, 306, 284
Mauas, P. J., Avrett, E. H., & Loeser, R. 1990, ApJ, 357, 279
Moore, R. L., & Rabin, D. M. 1985, ARA&A, 23, 239
Muchmore, D., & Ulmschneider, P. 1985, A&A, 142, 393
Musman, S., & Rust, D. M. 1970, Sol. Phys., 13, 261
Noyes, R. W., & Hall, D. N. B. 1972a, BAAS, 4, 389
———. 1972b, ApJ, 176, L89
Noyes, R. W., & Leighton, R. B. 1963, ApJ, 138, 631
Solanki, S. K., Livingston, W., & Ayres, T. 1994, Science, 263, 64
Thomas, J. H. 1985, Australian J. Phys., 38, 811

PLATE L4

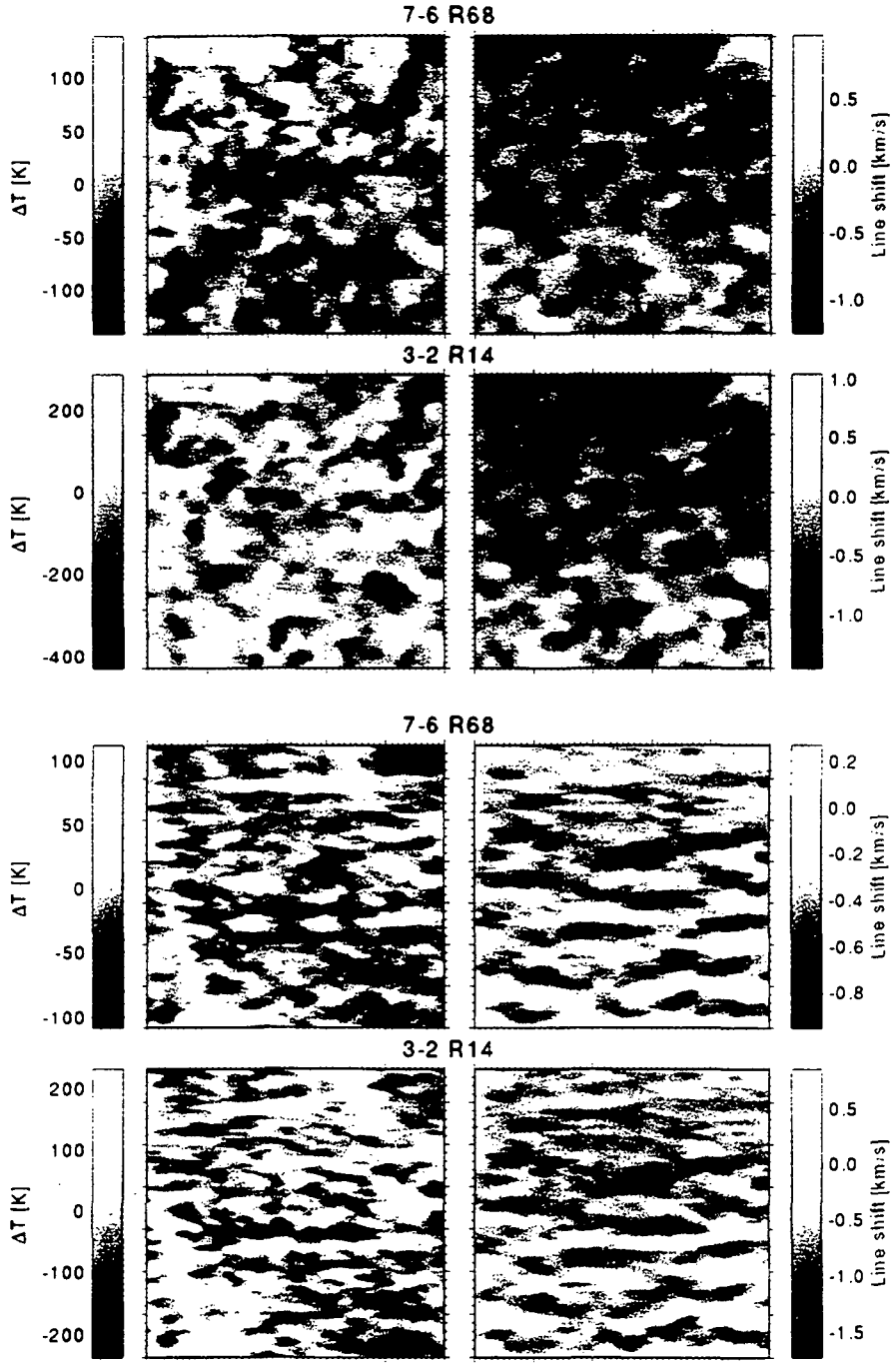

FIG. 1.—*Top two rows:* Temperature (*left-hand panels*) and Doppler shift maps (*right-hand panels*) of a quiet-Sun region in the weaker 7–6 R68 line and the strong 3–2 R14 line. Tick marks indicate 1″ intervals. The range of values in each map is indicated in gray-scale bars to the left and right. *Bottom two rows:* Space-time diagrams of variations in line-core temperature (*left-hand panels*) and Doppler shift (*right-hand panels*) of another quiet-Sun area. There are tick marks at 1″ intervals on the horizontal axis and at 1 minute intervals on the vertical axis.

UITENBROEK, NOYES, & RABIN (see 432, L68)

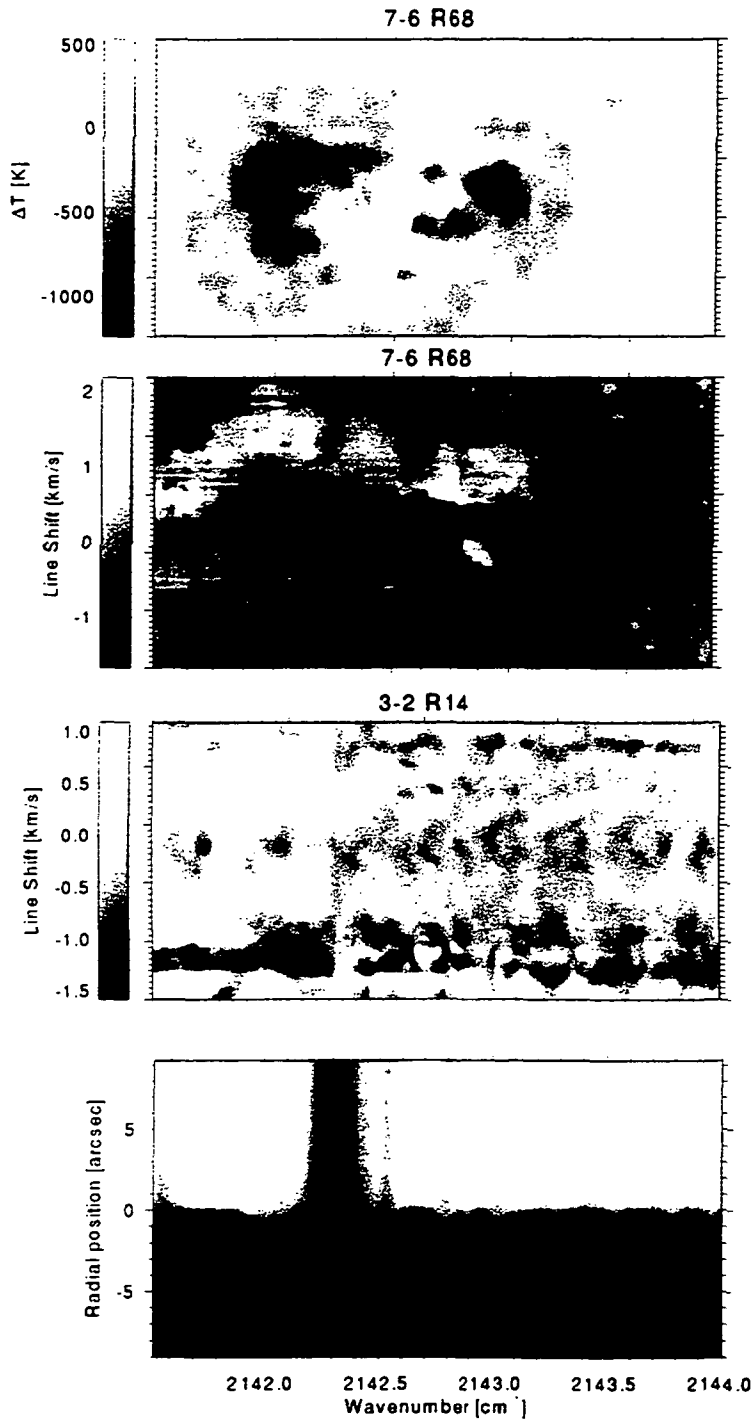

FIG. 3.—*Top panel:* Temperature-variation map of active region NOAA 7592 in the core of 7–6 R68. Heliographic north is toward the top; east is toward the left. Each small tick mark on the horizontal scale measures 5″: there are tick marks every arcsecond on the vertical scale. *Second panel:* Simultaneous map of Doppler shifts. *Third panel:* Space-time map of Doppler shifts in the strong 3–2 R14 line of the same region 2 days later. Time increases toward the right at 1 minute per tick mark: the vertical spatial scale is 1″ per tick mark. *Bottom panel:* Quiet-Sun spectrum at the limb.

From Chromospheric Dynamics, Proceedings of a mini-workshop held at Institute of Theoretical Astrophysics, University of Oslo, Norway, June 6-8, 1994, ed. Mats Carlsson.

NEW INSIGHT IN THE SOLAR T_{MIN} REGION FROM THE CO LINES AT 4.67 MICRON

HAN UITENBROEK and ROBERT W. NOYES
Harvard-Smithsonian Center for Astrophysics,
60 Garden Street, Cambridge MA 02138, USA

Abstract. We discuss recent observations of the fundamental vibration–rotation transitions of carbon monoxide (CO) in the solar infrared spectrum. Employing a new array detector at the McMath–Pierce facility on Kitt Peak we find that the CO lines sketch a rich picture of the dynamics of the solar temperature minimum region, the lower boundary of the chromosphere. In a spectra-spectroheliogram and a time-sequence of slit-spectra obtained during exceptional seeing conditions we observe small-scale bright, ring shaped, blueshifted features. We speculate that they are the signature of granular overshoot into the convectively stable temperature minimum. The centers of the rings are among the coolest elements seen in strong CO-line heliograms on the disk, and may be instrumental to the low temperatures observed in CO close to the solar limb.

Key words: CO molecule, temperature minimum, infrared, granulation

1. Introduction

Not many spectral diagnostics are available to study the structure and dynamics of the solar chromosphere. While our knowledge primarily stems from a few strong lines like the hydrogen Hα and Ca II H&K lines, most other lines have chromospheric contributions only close to the limb where accurate observations are difficult. Due to this lack of reliable observations we are currently not yet able to tell what the exact nature of the chromosphere is and what causes its temperature to rise from photospheric to (eventually) coronal values. Recent simulations by Carlsson and Stein (these proceedings) for instance suggest that the chromo"sphere" need not exist over the whole surface but rather represents moderately hot material that is locally and intermittently heated by outwardly propagating shock waves. With this in mind it is evident that we need to look for new observations that could confirm or discount the widely different models. It may seem unlikely that observations of molecular carbon monoxide (CO) lines provide us with such an opportunity, since all molecules dissociate at temperatures characteristic for the chromosphere. However, modeling any layer in the atmosphere requires a proper understanding of its boundary conditions. In the case of the solar chromosphere we are particularly interested in the amount of mechanical energy coming from the lower boundary, *i.e.*, the temperature minimum region, and lines of CO may play an important role precisely in diagnosing this energy flux and the form in which it is presented to the chromosphere.

In a static plane-parallel solar model both the balance of CO association and dissociation and the excitation–de-excitation equilibrium of the vibration-rotation transitions are dominated by collisions (Ayres and Wiedemann, 1989). Consequently, all relevant population are in thermodynamic equilibrium with local conditions (LTE),

and intensities map directly into temperatures. Surprisingly enough, CO observations close to the limb require temperatures as low as 3700—3800 K (Noyes and Hall, 1972a; Ayres and Testerman, 1981), values which are much lower than those predicted by models based on almost any other spectral diagnostic. A recently constructed model by Avrett (private communication) illustrates the discrepancy in thermal diagnostics clearly. The model fits disk-center intensities of several hundred CO lines in the ATMOS infrared atlas (Farmer and Norton, 1989), but predicts intensities that are far too low in such prominent spectral features as the Ca II H&K lines and the 150 nm and 100 μm continua which both originate from the same region. This failure of standard one-dimensional models to accommodate CO observations with other spectral diagnostics clearly calls for more intricate models of the solar atmosphere that include spatial inhomogeneities and/or time-dependent behavior. For this we need detailed observations that show when and where in the atmosphere the lowest CO temperatures occur. In Sect. 3 we discuss our continuing effort to do such observations with the McMath-Pierce solar telescope at Kitt Peak. First we briefly discuss the instrumental setup in Sect. 2, while we present our conclusion in Sect. 4.

2. Observational parameters

Infrared CO spectra at 4.67 μm have been available with good spectral resolution for more than twenty years (Noyes and Hall, 1972a; 1972b). Until recently, however, the lack of array detectors has severely limited the spatial resolution that could be achieved at such long wavelengths. This changed with the advent of a new infrared array detector at the NSO McMath–Pierce facility on Kitt Peak. A comprehensive description of the instrument and observational parameters for our first set of observations with the infrared array in October 1993 can be found in Uitenbroek *et al.* (1994). The first results of this run show the CO lines to be very exciting lines rich in information. In this section we briefly mention improvements in the instrumental setup for a second observation run in May 1994. New results are discussed in the next section.

The diffraction limited resolution of the 1.5 m McMath-Pierce main telescope is 0.″77 at 4.6 μm. The vertical spectrograph with infrared grating and 220 μm wide slit achieves a resolution of $\Delta\lambda/\lambda = 90\,000$. The detector is a 256×256 InSb array with an adjustable readout rate which was usually set to 7 Hz. In our second observing run (May 1994) we used minifying optics to compress the image in the spatial direction and expand the field of view by a factor of two to approximately 100″ with a 0.″38/per pixel resolution. Addition of an optical disk allowed us to increase the data throughput of the system and achieve a cadence of 2 seconds per frame, an improvement of more than a factor of 2 over the first observations in October 1993.

In Fig. 1 we display a sample spectrum of a quiet-Sun region on the disk (cosine of the viewing angle $\mu = 0.5$). This spectral region represents one of the few infrared windows through the earth atmosphere with little contamination of terrestrial lines. It contains several strong and weak (*i.e.* low and high excitation) lines. We will use the 3-2 R14 in this window as representative for stronger CO lines, and the 7-6 R68

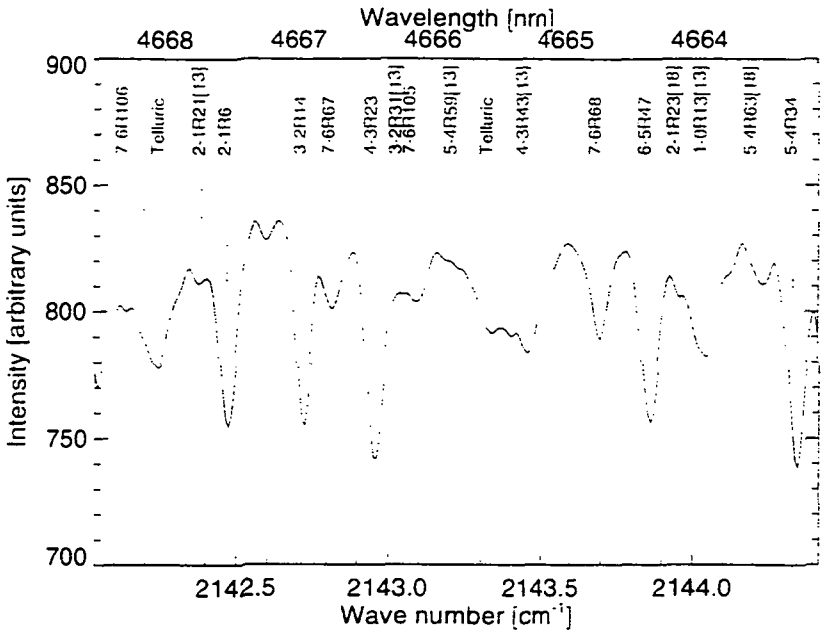

Fig. 1. A sample solar CO spectrum from a quiet area at $\mu = 0.5$. Lines marked with [13] refer to lines from the ^{13}CO isotope; those marked with [18] to lines that arise from $^{12}C^{18}O$.

line as representative for weaker lines because they are relatively less blended with other lines.

We used the instrument in two different modes of observation: one stresses resolution in space, the other resolution in time. In the first mode we scanned the solar surface with the slit to build spectra-spectroheliograms, data cubes that allow us to make two-dimensional spatial maps of any function of wavelength such as the intensity in a stretch of continuum, the core of a certain line, or a line's Doppler shift. In the second mode we took time-sequences of spectra at a fixed position on the surface and recorded temporal variations of spectral quantities along the slit. To construct line-intensity maps and Doppler maps we made parabolic fits to the lowest three points of the line profile at each position of a space-space or space-time scan, and determined the value at and the position of the minimum of the fitted profile. Doppler shifts in the displays of Figs. 2—4 are specified with respect to the average position of the line, with blue shift (corresponding to upward mass motion) coded light and redshift coded dark.

3. Results

The picture of the temperature minimum region that emerges from time and space resolved spectroscopy of the infrared CO lines is a very dynamical one. Our first observations with the infrared array (Uitenbroek *et al.*, 1994) showed that, at disk center, line shifts variations have a dominant period of 5 minutes, spatial scales of 10–20″, and typical RMS amplitudes of 0.3–0.4 km/s. Line-core intensities of the stronger lines exhibit more the character of the chromospheric 3-minute oscillations with a smaller spatial scale of 3–5″, and RMS variations that correspond to 90 K

temperature fluctuations. Higher up in the temperature minimum region the spatial distribution of temperatures appears asymmetric with an extended tail towards small-scale cold elements. The magnetic network could be tentatively identified (as bright elements) in the intensity maps, but this could not be substantiated since we did not have co-spatial Ca II K line images during the October 1993 run. The network did not seem to have a clear signature in maps of line shift.

We now turn to a discussion of two sets of observations that were obtained on May 6, 1994 under very favorable seeing conditions. Judging from the smallest scale elements in our data the atmospheric seeing must have been at the diffraction limit of the telescope at 4.67 μm or better. The telescope was positioned on a quiet area at heliographic position 12N, 62E (corresponding to a viewing angle of 60 degrees, or $\mu = 0.5$) with an East–West oriented slit. We first obtained a time-sequence of 1200 spectra at 2.2 second intervals and then obtained a $100'' \times 100''$ spatial scan (200 spectra at $0''.5$ spacing) centered on the surface position of the preceding time-sequence. Between the time-sequence and the spectra-spectroheliogram we obtained a co-spatial Ca II K-line filtergram with a wide bandpass centered on the core of the line. This allows us now to unambiguously identify network elements.

Figure 2 shows three space-time maps extracted ¿from the time-sequence of spectra. It contains two maps of temperature fluctuations as derived from continuum intensity variations (left panel) and variations in 3-2 R14 line-core intensity (middle panel) respectively, and a space-time map of 3-2 R14 line-core shift (right panel). In order to do justice to the high spatial and temporal resolution of the present data we display only the first half of the sequence. At around 6 and 22 minutes after the start of the sequence clouds passed over giving rise to the dark bands which are especially visible in the low contrast continuum map (left panel, Fig. 2). In the line-shift map the passing clouds cause a temporary loss of resolution. Because the left side of the slit was oriented towards the (East) limb the continuum map shows the effect of limb darkening towards that end, while the difference in projection of solar rotation velocity in the line of sight between both sides of the slit (≈ 0.2 km/s) gives rise to a Doppler map that is, on average, slightly darker (*i.e.* more red shifted) on the left (limb-ward) side.

The bright vertical lines at horizontal positions $33''$ and $64''$ in the continuum and line intensity maps of Fig. 2 are network elements. They are easy to identify in the K-line filtergram (upper left panel Fig. 4). The location of the network is not readily identified in the Doppler map. Compared to our previous observations (Uitenbroek *et al.*, 1994, Fig. 3 therein) we note several important differences. The favorable seeing conditions allow us to see a fine-scale pattern with structures as small as $1''$, that reminds us of the photospheric granulation: bright streaks that last for several minutes and that sometimes diverge, sometimes converge. The streaks, which often appear in pairs correspond to blueshifted material in the Doppler map, where they sometimes seem to merge into more fuzzy blobs of blue-shifted (coded bright here) material. Since the spectrograph slit renders a one-dimensional cross-section of the solar surface, the streaks most likely represent ring shaped (although not necessarily circular) structures. The typical separation of 3-5$''$of the bright streaks is slightly larger than the cell size of photospheric granulation, but corresponds perhaps to the strongest granules overshooting in the stable temperature minimum

region These appear as "exploding" granules in photospheric granulation movies (Title *et al.*, 1989). In between the bright streaks there are sometimes dark single streaks that last for about 2 minutes. These intermediate dark narrow elements are among the darkest elements in the time-sequence. reminiscent of the centers of large granules that cool strongly due to the adiabatic expansion of upflowing material in the exponentially stratified atmosphere in theoretical granulation simulations (*e.g.* Stein and Nordlund, 1989). It is likely that a similar picture as seen in CO line intensity is observed in the spectra of the Ca II K-line wings that originate from the same altitude. We are reminded of the effect, first observed by Evans and Catalano (1972), in which granulation contrast inverts between K-line wing intensities and continuum intensity where granular centers are bright.

We remark that the peak-to-peak temperature variations of approximately 400 K seem to differ little between observations with very different seeing conditions (*cf.* the lower left panel in Fig. 3 of Uitenbroek *et al.*, 1994, and the middle panel of Fig. 2). Thus, we do not expect real fluctuations to be much larger. By contrast, the peak-to-peak velocity variations at the viewing angle of $\mu = 0.5$ of the present data are a factor of 2 higher than those observed at disk center under less favorable seeing conditions. This indicates that either small-scale velocity variations partially cancel out when the image is blurred, or that the velocity distribution is strongly dependent on viewing angle. The latter would mean that horizontal velocities would be larger than vertical. Although this does not conform with measured microturbulence (which is a proxy for the average small-scale velocity fields) derived from photospheric lines which shows exactly the opposite behavior (*cf.*, Rutten and Milkey, 1979), it agrees with simulations of solar granulation which show strong expansion flows in horizontal directions (Steffen and Muchmore, 1988; Stein and Nordlund, 1989). (Further observations, of course, will resolve this issue.)

The time slices in Fig. 2 display a lot of detail that make them difficult to analyze. They represent a superposition of at least two modulating phenomena: the granulation with small spatial scales and time-scales of up to 10 minutes, and the response of the temperature minimum region to the global 5-minute P-mode oscillations. We attempted to separate these effects by filtering the time-slices in space and time. The result is displayed in Fig. 3 where the bottom two panels show the time-slices of temperature variation (left panel) and line shift (right panel) of the 3-2 R14 line filtered with a temporal passband of 3-5 minutes and spatial low-pass filter with a cutoff at 10″. The top two panels were constructed by removing the bottom two slices ¿from the total signal as displayed in the middle and right panels of Fig. 2.

Correlating the two 3-5 minute band slices we find that redshift leads maximum temperature by 50 seconds (*i.e.*, approximately 90 degrees in phase, as expected for an adiabatic standing wave). Note that the distribution of line shifts in the lower right image is symmetric around zero, while that of the upper right slice is skewed to larger positive values (blue shift). These have a relatively small filling factor since the zero level is defined as the average velocity over the whole slice. The topology of the "granulation" slice, therefore, has small areas with relatively strong blue shift embedded in larger areas of relatively mild redshift. Most sharply defined blueshifted areas correlate with bright areas in the 3-2 R14 temperature map, although there

is not a well-defined one-to-one correspondence. This may be due to the relatively large viewing angle of 60 degrees which causes considerable projection effects.

After the time-sequence displayed in Fig.2 we obtained a K-line filtergram and CO spectra-spectroheliogram of the same area. Figure 4 shows three spatial maps extracted ¿from the heliogram, which was centered on the slit position of the time-sequence. The corresponding subarea of the K filtergram is shown in the lower right panel with the slit position of the the preceding time-sequence overplotted. The other three panels of Fig. 4 display the 3-2 R14 temperature map (upper left panel), continuum temperature map (upper right), and the 3-2 R14 Doppler shift map (lower left). The continuum and 3-2 R14 maps are all co-spatial and simultaneous on a horizontal line-by-line basis; it takes 440 seconds to build up the whole heliogram scanning the slit over the surface. The K-line filtergram appears to be considerably more blurred than the CO heliograms, probably due to the worse seeing at the shorter wavelength of the K line.

Some bright patches of network appear in the temperature heliograms. Their position is easily confirmed from the K-line filtergram. The brightest two in the middle of the images correspond to the bright vertical stripes in the temperature maps of Fig.2. Confirming our earlier remark, the network is not recognized in the 3-2 R14 Doppler map (lower left panel). The Doppler map is characterized by small scale bright (blue-shifted) patches of 2–3″ size, and a larger scale checker-board pattern of 15–20″. The latter is characteristic of the 5-minute oscillation.

It is difficult to recognize the ring-shaped patterns suggested by the space-time maps in the heliograms. This may be due to a fragmentation of overshooting granules that is also visible as a break-up of exploding granules in photospheric movies (Title *et al.*, 1989). Ideally we would like to be able to obtain series of heliograms at small enough time intervals to confirm our impressions. Unfortunately, the current setup does not allow the required high data rate.

4. Conclusion

We were fortunate to encounter very favorable seeing conditions during part of our May 1994 observation run. The obtained CO data reveal an even more intricate picture of the temperature minimum region then we suspected from our previous infrared array observations. A time-sequence that we obtained shows bright streaks associated with blue-shifted material. We tentatively identify the ring-like structures that the streaks imply with the signature of granular flow. We would like to remark that the picture we sketch is not in conflict with the topology of granular flow as sketched by Stein and Nordlund (1989) who describe the top layer of the granulation flow as having broad, slow, up-flow regions and confined fast down flows. The latter picture refers to the situation beneath the photosphere, invisible to us at any wavelength. Rather, we speculate that in CO we observe occasionally strong granules that overshoot into the stable temperature minimum region and give rise to localized up-flow regions, which appear sometimes as ring-shaped temperature enhancements, sometimes as bright blobs in the temperature maps, embedded in a more uniform medium that is dominated by the 3-5 minute oscillations. In this picture the rapidly expanding granule interiors give rise to small scale cold areas

that appear as dark streaks lasting for 1-2 minutes in CO time slices. These cold areas could play an important role in the low CO temperatures that are observed at the solar limb by creating a shadowing effect in which they obscure hotter material in the line of sight due to their larger CO abundance.

Acknowledgements. We would like to thank Doug Rabin and Dave Jaksha for help with the observations, and Gene Avrett for fruitful discussions. This work was supported in part through NASA grant NAGW-2545. H.U. thanks the University of Oslo for making it possible to attend the workshop in Oslo.

References

Ayres, T. R. and Testerman, L.: 1981, *Astrophys. J.* **245**, 1124
Ayres, T. R. and Wiedemann, G. R.: 1989, *Astrophys. J.* **338**, 1033
Evans, J. W. and Catalano, C. P.: 1972, *Sol. Phys.* **27**, 299
Farmer, C. B. and Norton, R. H.: 1989, *A High-Resolution Atlas of the Infrared Spectrum of the Sun and the Earth Atmosphere from Space*, NASA Ref. Pub. 1224, Vol 1
Noyes, R. W. and Hall, D. N. B.: 1972a, *Bull. Am. Astron. Soc.* **4**, 389
Noyes, R. W. and Hall, D. N. B.: 1972b, *Astrophys. J. Lett.* **176**, L89
Rutten, R. J. and Milkey, R. W.: 1979, *Astrophys. J.* **231**, 277
Steffen, M. and Muchmore, D.: 1988, *Astron. Astrophys.* **193**, 281
Stein, R. F. and Nordlund, Å.: 1989, *Astrophys. J. Lett.* **342**, L95
Title, A. M., Tarbell, T. D., Topka, K. P., Ferguson, S. H., Shine, R. A., and the SOUP Team: 1989, in R. J. Rutten and G. Severino (Eds.), *Solar and Stellar Granulation*, NATO ASI Series C-263, Kluwer, Dordrecht, p. 225
Uitenbroek, H., Noyes, R. W., and Rabin, D. M.: 1994, *Astrophys. J. Lett.* in press

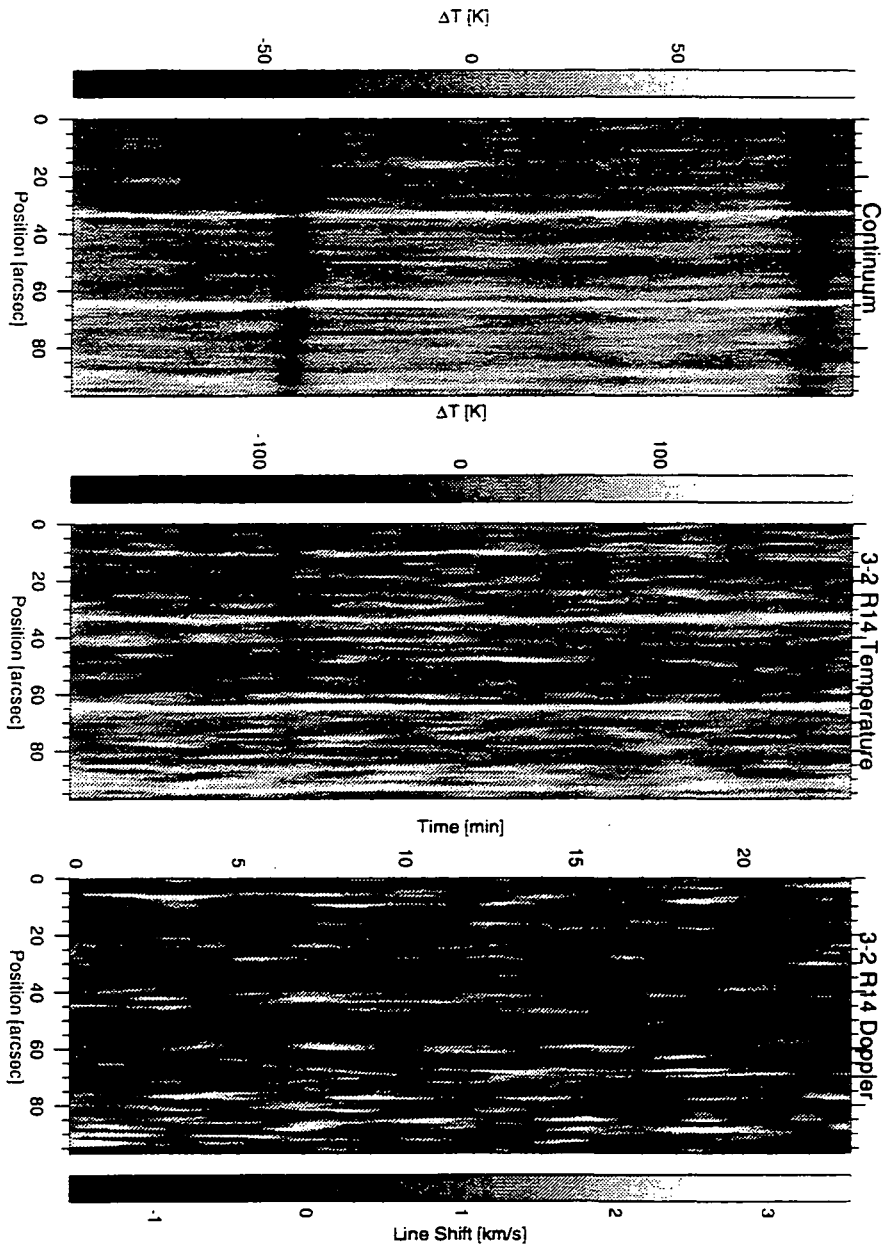

Fig. 2. Space-time maps of infrared continuum variations (left panel), and 3-2 R14 line-core temperature and line-shift variations (middle and right panels respectively).

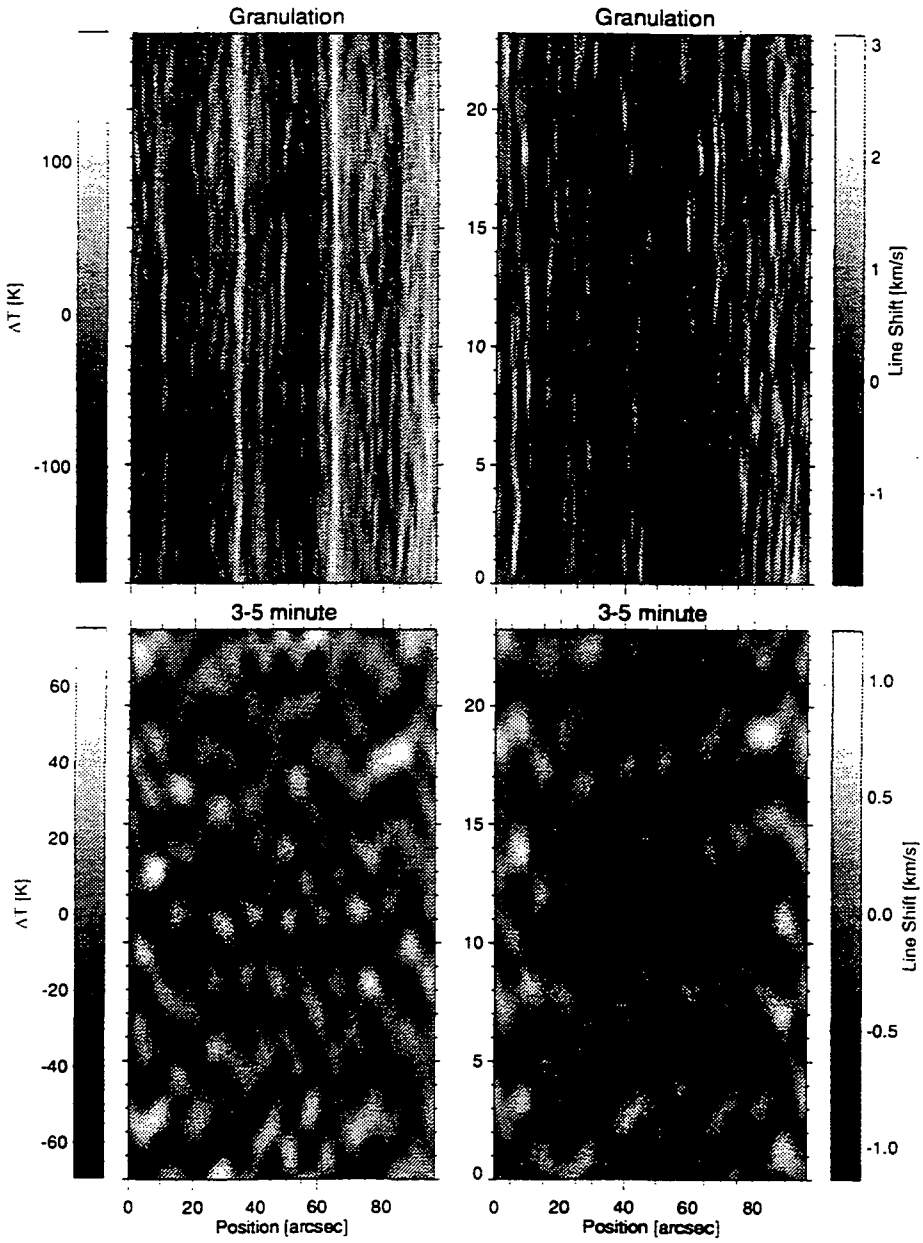

Fig. 3. Filtered time-slices of the 3-2 R14 temperature (left panels) and line shift (right panels) variations. Lower panels are filtered with a 3-5 minute temporal bandpass and a spatial lowpass filter with 10″ cutoff. Upper panels show slices more chracteristic for the spatial and temporal behaviour of granulation with 3-5 minute band removed.

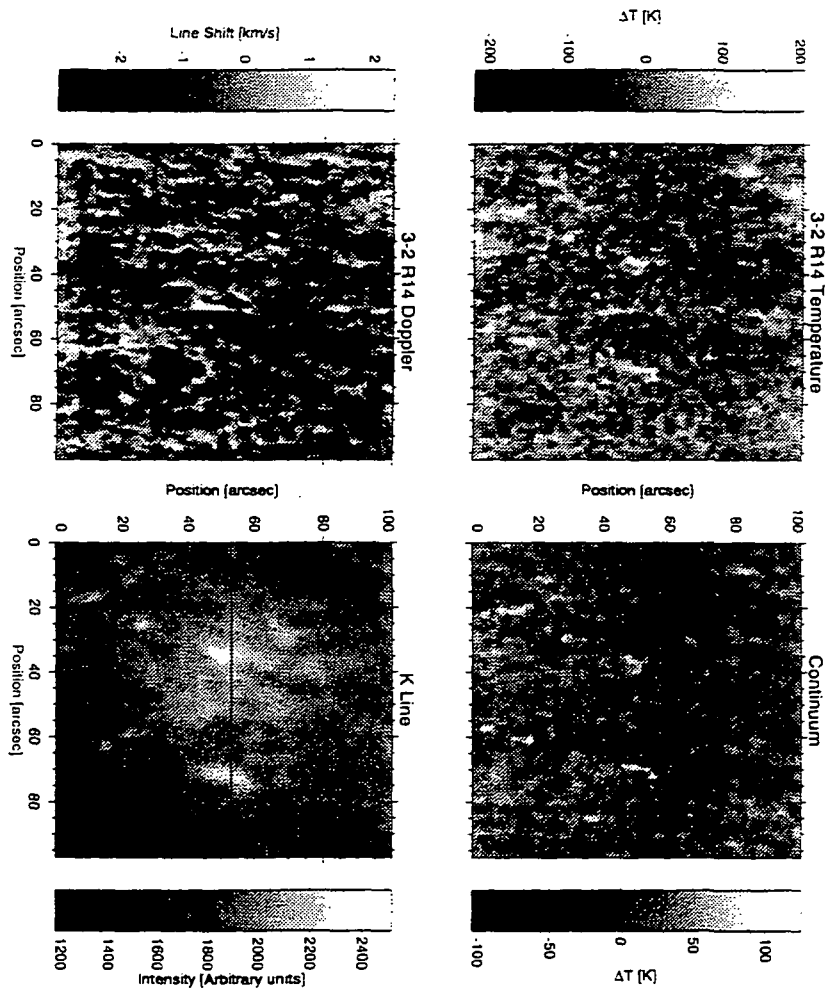

Fig. 4. Heliograms of Ca II K-line core intensity (lower right panel), infrared continuum temperature variations (upper right), 3-2 R14 line shift (lower left), and 3-2 R14 line-center temperature variations (upper left panel). Horizontal line in the K-line filtergram indicates the position of the slit for the preceding time-sequence (see Fig. 2).

THE ASTROPHYSICAL JOURNAL, 447:419–427, 1995 July 1

VORTICITY AND DIVERGENCE IN THE SOLAR PHOTOSPHERE

YI WANG,[1] ROBERT W. NOYES,[1,2] THEODORE D. TARBELL,[3] AND ALAN M. TITLE[3]
Received 1994 November 7; accepted 1995 January 17

ABSTRACT

We have studied an outstanding sequence of continuum images of the solar granulation from Pic du Midi Observatory. We have calculated the horizontal vector flow field using a correlation tracking algorithm, and from this determined three scalar fields: the vertical component of the curl, the horizontal divergence, and the horizontal flow speed. The divergence field has substantially longer coherence time and more power than does the curl field. Statistically, curl is better correlated with regions of negative divergence—that is, the vertical vorticity is higher in downflow regions, suggesting excess vorticity in intergranular lanes. The average value of the divergence is largest (i.e., outflow is largest) where the horizontal speed is large; we associate these regions with exploding granules. A numerical simulation of general convection also shows similar statistical differences between curl and divergence. Some individual small bright points in the granulation pattern show large local vorticities.

Subject headings: hydrodynamics—Sun: atmosphere — Sun: granulation

1. INTRODUCTION

Motions of magnetic footpoints are thought to be closely related to heating in the upper solar atmosphere (Sturrock & Uchida 1981; Zirker & Cleveland 1993). Motions of magnetic fields appear to be closely related to convective flows in the photosphere, as revealed by the continuously changing patterns of solar granulation. Studies of the flows in the photosphere are important for obtaining a better understanding of the magnetic heating process. Other stars on and off lower main sequence, which exhibit all the phenomena of solar magnetic activity and atmospheric heating, have atmospheres that are probably energized in a very similar way. Yet the Sun is the only star for which we have the possibility, in the foreseeable future, to study the interaction of convection and magnetic fields at the relevant spatial scale—which in the solar photosphere is roughly one density scale height, of the order 100 km. Therefore detailed study of the flow fields in the solar photosphere can provide us with important insights about the outer atmosphere of stars.

Only with data of the highest spatial resolution free of atmospheric seeing distortions can we determine the true horizontal flow field in the solar photosphere. Though limited in the number of images and duration, such a data set was obtained by the Solar Optical Universal Polarimeter (SOUP) aboard the 1985 Spacelab 2 space shuttle flight (Title et al. 1986). These images have been used to study the statistical properties of solar granulation (Title et al. 1989), the transport of magnetic fields by horizontal flows (Simon et al. 1988), and temporal properties of horizontal velocities and their associated divergence and curl (Tarbell et al. 1992). Aside from the above-mentioned data set, no other time series of high-resolution images from space is available. However, ground-based data can in principle yield higher resolution (because of the larger optics of ground-based telescopes) provided the degradation caused by seeing can be overcome. Destretching can be used to remove atmospheric seeing distortions in ground-based images (November 1986; Topka, Tarbell, & Title 1986). Destretched high-resolution images from Pic du Midi observatory in France, and from the Swedish Solar Telescope at La Palma in the Canary Islands have become valuable tools for studying dynamics at the solar surface.

The rich dynamics of the solar photosphere makes the extraction of flow fields a complicated process even with seeing-free data. Solar p-mode oscillations, surface waves, motions regulated by the magnetic field, motions due to mesogranulation and supergranulation, all enter into the picture we are trying to understand. The subfundamental Fourier filter (Title et al. 1992) developed at Lockheed Palo Alto Research Laboratories (LPARL) has been applied to both ground-based data and those obtained in space to remove the effect of solar oscillations. A filtered high-resolution movie shows high stability with little effects from solar oscillations and is suitable for studying horizontal flows in the solar surface.

An effective method for studying horizontal motions at the solar surface is local correlation tracking (LCT; November & Simon 1988). This is an extension of "destretching" of successive solar images to remove distortions induced by atmospheric seeing. LCT uses a finer grid to track solar features and calculate their frame-to-frame motion. Unfortunately, the image motion caused by seeing is indistinguishable from solar flows in a single measurement. The seeing distortion has a correlation time of a fraction of a second, and appears as a "white" noise source with a flat temporal spectrum. Therefore, if the solar motions are oversampled in time, the seeing distortions can be reduced by simple averaging. This process however is complicated by the evolution of solar features, most notably granules, with characteristic timescales of a few minutes. The method is most effective with data sets whose cadence is short compared to that timescale.

Using images taken at Pic du Midi Observatory and processed at LPARL, Muller & Roudier (1992) have studied the evolution of network bright points (NBP), and Muller et al.

[1] Department of Astronomy, Harvard University, 60 Garden Street, Cambridge, MA 02138
[2] Smithsonian Astrophysical Observatory, 60 Garden Street, Cambridge, MR 02138.
[3] Lockheed Palo Alto Research Laboratories, 3251 Hanover Street, Palo Alto, CA 94304-1121.

(1992) have studied evolution and advection of mesogranulation. Brandt et al. (1988) have found vortex flows on a scale larger than the granulation in a sequence of images obtained at the Swedish Solar Telescope in La Palma. Similar data have also been used in modeling exploding granules (Simon, Title, & Weiss 1991).

In this paper we study three scalar fields in the photosphere, using images obtained at Pic du Midi Observatory. We calculate the vertical component of the vorticity, $(\nabla \times v)_z$, which we call Curl, the divergence of the horizontal flow ($\nabla \cdot v_h$), called Div, and horizontal flow speed ($|v_h|$), called speed. A convection simulation of Porter, Woodward, & Mei (1991) is also analyzed, using the same analysis techniques. The Pic du Midi data set is among the best available, although it suffers from lack of correlative line of sight velocity and magnetic data, with limited linearity, being digitized from photographic plates. Destretching is first used to reduce distortions due to "seeing" between successive frames. Then a subfundamental filter is applied to one of the data sets to remove motions due to solar p-mode oscillations and further reduce the noise level. These processed images can then be used to derive horizontal flows associated with solar convection using LCT.

The next section provides detailed information on the data used in this paper and discusses the sources of noise in these data sets. Section 3 deals with the horizontal vector flow fields and associated flow speed distribution. Section 4 discusses the spatial and temporal properties of Div and Curl fields derived from the flow fields, while the relationship between Div and Curl fields is discussed in § 4. In § 5, we discuss high-velocity rotational motion of a pair of NBPs in the Pic du Midi data. Further discussion and conclusions are given in § 6.

2. DATA AND ANALYSIS

Three sets of data are studied: two subsets of the Pic du Midi data called WL and GD, and a nonlinear compressible three-dimensional simulation of generalized convection. The rationale for analyzing three separate data sets is as follows: the WL data were chosen because they have been subfundamental filtered to remove the effects of the 5 minute oscillation, thus revealing the residual convective flow field more clearly. Because of concern that the filtering process might affect the apparent properties of the residual flow field, we also analyzed the GD data set, which is an unfiltered (and longer) data set from the same observing sequence. The simulation data set was analyzed to see to what extent our findings are also present in numerical simulations of convection, and thus whether our findings are general properties of convection or specific to solar conditions. The WL data set, however, serves as the primary data set in this study. Table 1 provides details of the data sets.

1. The WL data set contains 526 continuum (5750 Å) ultra–high-resolution images near disk center, taken by R. Muller at Pic du Midi Observatory with the 50 cm refractor, on 1988 September 20. Every 20 seconds a set of 50 burst images was taken by a high-speed film camera (Muller & Roudier 1992). One frame with the best image quality over a selected region is selected in each burst set. Thus on average each successive frame in the WL series is separated by 20 seconds. Seeing was excellent throughout the observation and diffraction limit was approached across the field of view in almost every selected frame. The WL series was digitized at LPARL at 0.065 arcsec pixel^{-1}, with 1024^2 pixel (66.56^2 arcsec^2) in the field, spanning 2 hr 55 minutes. We have analyzed a subsection of the WL series containing 480^2 pixel (31.2^2 arcsec^2) in size, spanning 57 minutes. These images were rigidly aligned, and then destretched to remove atmospheric seeing distortions. The subfundamental filter was then applied to remove brightness variations due to the 5 minute p-mode oscillations.

This portion of the WL data set has been analyzed before by Muller & Roudier (1992). Muller et al. (1992) also analyzed the full WL data set and generated flow maps using LCT. We independently used LCT to calculate the horizontal flow fields from the positional difference of the local brightness pattern between two image frames, but at different resolution from Muller et al. The window for our flow maps is a truncated Gaussian with FWHM of 10 pixels (0.65 arcsec) and a cutoff of 20 pixels. The spacing between the location of the flow field vectors is 10 pixels.

2. The comparison GD data set had previously been digitized from the same raw data set as was used for the WL data, but for another purpose. Compared to the WL data, the spatial position of the GD data was slightly different, the pixel size about double (0.1415 arcsec), and the number of pixels in each direction (512) half as great, so that the area covered (72.45^2 arcsec^2) was similar. The GD data had been aligned and destretched. However, the data are substantially more noisy than the WL data due to lack of Fourier filtering. Flow maps had also been generated for the GD data set using LCT. The resolution of these flow maps corresponds to a truncated Gaussian with FWHM of 1.132 arcsec (8 pixels). While the portion of WL data set we used has significantly better spatial resolution and signal-to-noise ratio (SNR), the GD data set is 3 times longer in time.

3. We have studied a three-dimensional compressible convection simulation set calculated using the Piecewise-Parabolic Method (Porter, Woodward, & Mei 1991), provided to us by N. Hurlburt. The simulation spanned six pressure scale heights and had an array size in x, y, and time of (200, 200, 100). The numerical scheme solves the inviscid Euler equations, and hence has no formally defined viscosity. Thus the Rayleigh and Reynolds numbers are formally infinite. While the simulation is not meant to reproduce solar conditions, nevertheless it does allow us to compare our findings with some general properties of convective flows. The flow fields provided in the simulation are noise-free.

Each flow field in a given set of data will have three associated scalar fields: Div, Curl, and speed. The Div and Curl,

TABLE 1

INFORMATION FOR EACH DATA SET USED

Data Sets	Pixel Resolution	Time Resolution (s)	Flow Resolution	Size of Arrays (x, y, t)	Field of View	Duration
Pic du Midi, WL.....	0".065	20	0".65	(480, 480, 172)	31".20	57 minutes
Pic du Midi, GD.....	0".1415	20	1".132	(512, 512, 525)	72".45	2 hr, 55 minutes

fields are calculated in the following way:

$$\mathrm{Div} = \frac{\partial v_x}{\partial x} + \frac{\partial v_y}{\partial y} = \frac{v_x(x + \Delta x) - v_x(x - \Delta x)}{2\Delta x} + \frac{v_y(y + \Delta y) - v_y(y - \Delta y)}{2\Delta y} \quad (1)$$

$$\mathrm{Curl}_z = \frac{\partial v_y}{\partial x} - \frac{\partial v_x}{\partial y} = \frac{v_y(x + \Delta x) - v_y(x - \Delta x)}{2\Delta x} - \frac{v_x(y + \Delta y) - v_x(y - \Delta y)}{2\Delta y} \quad (2)$$

where Δx and Δy correspond to the spacing of points in the flow field calculation. We therefore calculate Div and Curl locally at each point using the four nearest points in the flow field. Note that the difference between the Div and Curl calculations lies simply in the projection of the flow field vectors at the four nearest points; any random (noise) component of the flow field should cause identical effects in the Div and Curl calculations. We will compare the properties of Div and Curl in § 4.

In calculating Div, Curl, and speed for the simulation data, we simply used the values of v_x and v_y provided by the simulation, rather than applying correlation tracking to the time-varying intensity field of the simulation.

There are three major sources of error in convective flows determined from the observed data. The first is noise due to nonlinear combination of distortions and scintillation that survived the destretching procedure. In unfiltered data this is by far the dominant source of noise, but it is drastically reduced in the subfundamental-filtered WL data. The second source of noise is the effect of solar p-mode oscillations. This also is present in the unfiltered GD data set but is largely eliminated in the subfundamental-filtered WL data. A third source of error arises from evolution of the granulation pattern: since correlation tracking assumes that all shifts in the cross-correlation peak are caused by mass flows on the sun, anisotropic intensity evolution can cause errors in flows determined using correlation tracking. For the GD flow maps which were derived from unfiltered data sets, we can significantly improve the SNR by averaging a large number of adjacent frames together, at the expense of introducing some noise from evolution of features. As we show immediately below, averaging 16 successive frames significantly enhances the SNR, while preserving enough time resolution for our main purpose of testing whether the findings from the primary WL data set are affected by the filtering process.

In order to investigate the effect of the random noise, we generated a Gaussian random displacement field representing the x-component of the displacement derived from correlation tracking, assuming it to be pure Gaussian noise. We then derived a flow vector, v_x, by taking the difference between each pair of successive random displacement fields. We have scaled the random flow so that it has the same single-frame rms v_x as for the GD data—namely 4.3 km s^{-1}, i.e., we assume that this extremely high value is essentially all due to noise. We then calculated the rms of v_x for both the GD data and the Gaussian random flow field after averaging 2^n adjacent frames together and compared their differences. Figure 1 shows the rms of v_x for both the WL (filtered) and GD flows, and the random Gaussian flow. We note that the filtered WL flow fields have a single-frame rms v_x of 0.8 km s^{-1}, and the rms decreases very slowly with averaging. Averaging the GD velocity frames makes the GD rms v_x converge onto the WL values, while averaging the Gaussian noise frames causes their rms v_x to converge to zero. Averaging 16 frames of GD data yields an rms velocity about 2.5 times that in the 16-frame averaged Gaussian noise data; that is, a SNR of about 1.5. The following analyses of the GD data are performed on 16-frame averaged data. The WL data set, being processed by the subfundamental filter, have a very high single-frame SNR and thus are analyzed without averaging.

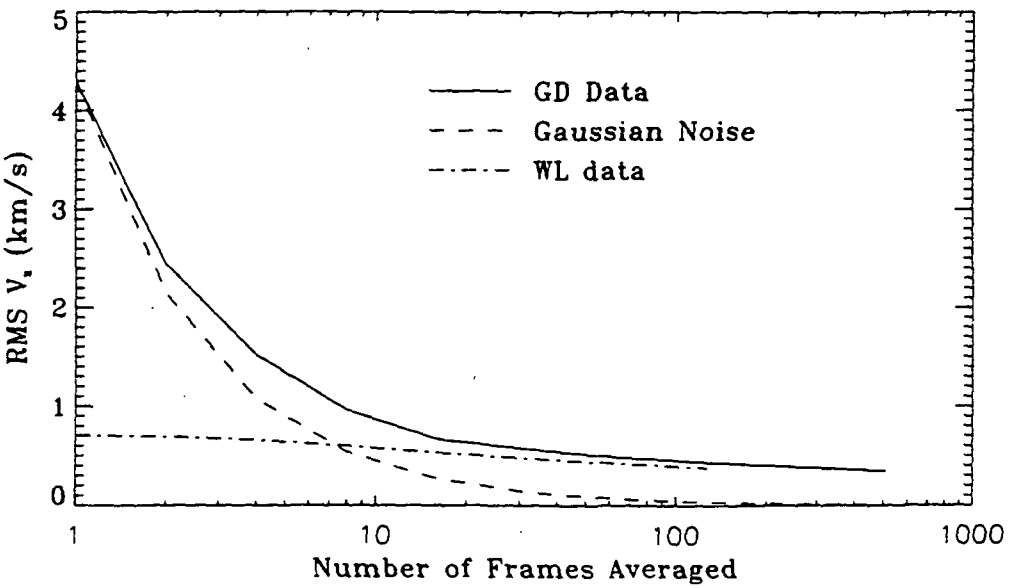

FIG. 1.—Root-mean-square of x-component of the flow speed in the Pic du Midi GD and WL series. Averages of 2^n frames are taken before the rms calculation. The solid curve denotes the observed rms in the GD data, the short dashed line denotes the rms from a Gaussian random flow field, and the dash-dotted line shows the WL data. It is apparent from the plot that the WL series is signal dominated while averages of at least 10 frames must be taken to substantially reduce the noise level in the GD data.

3. GENERAL FLOW FIELD PROPERTIES

We have found that the distribution of horizontal flow speeds as measured either from the WL flow field or the 16-frame averaged GD flow field closely approximates a two-dimensional Maxwellian (or Rayleigh) distribution. This is shown in Figure 2. The nonlinear best fit of a two-dimensional Maxwellian distribution to the GD distribution is plotted with the data. The most probable speed is about 0.65 km s^{-1}. Note that the WL and GD data give essentially the same results. The slightly lower mean of the GD speed is probably caused by the decorrelation of solar signals in 320 s while the WL speed does not suffer from such an effect. We have calculated the same speed distribution function for the simulation data, and find that it too approximates a two-dimensional Maxwellian distribution.

A two-dimensional Maxwellian speed distribution is what would be expected if the horizontal x- and y-components of the velocity field each had Gaussian distributions. Because both the simulation and the observed flow fields show this effect, we suspect that this relationship is a real, if not obviously expected, property of turbulent convection. We note that a most probable value for the flow speed of 0.65 km s^{-1} could be somewhat of an overestimate, since there is still some residual noise in both flow fields.

The distribution of flow field vectors themselves as revealed by the WL data shows a gradually evolving pattern of large-scale flow. Figure 3 shows the mean flow field averaged over the 57 minutes of the WL data series. The maximum mean speed is 1.25 km s^{-1} and the rms speed is 0.53 km s^{-1}. It is clear that over this time span the time-averaged flow is spatially coherent. There are clearly defined mesogranular structures, as already described by Muller et al. (1992). A number of regions can be identified as having persistent outflows, such as the ones at the upper left and lower right corners in Figure 3. These regions are associated with reoccurrence of exploding granules, consistent with the findings of Simon et al. (1991). Naturally they also have large average value of Div over time. Regions of persistent outflow are also seen in the average flow fields of the GD series, indicating that they can last at least as long as 3 hours. A lifetime at least this long is not surprising, since it would take about 10 hours for mesogranules to be

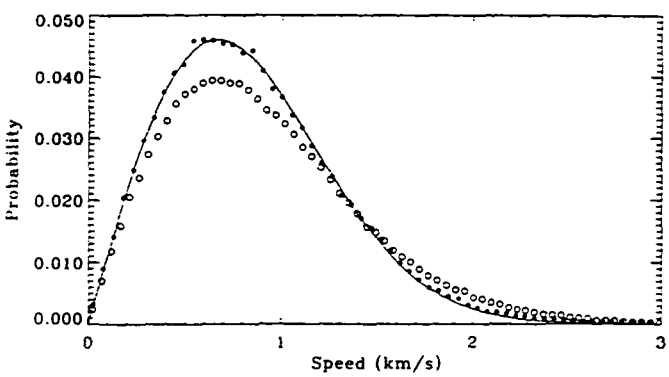

FIG. 2.—Distribution of speeds in the Pic du Midi data. Dots represent the 16 frame averaged GD data while the curve represents the nonlinear best fit of a two-dimensional Maxwellian Distribution. Open circles represent the distribution of the WL data. This shows that by averaging 16 frames in the GD data, we have obtained a flow field very similar to that of the subfundamentally filtered WL data. Since the speed data is dominated by a real solar signal, we conclude that the distribution of speed in the solar photosphere closely resembles a two-dimensional Maxwellian distribution.

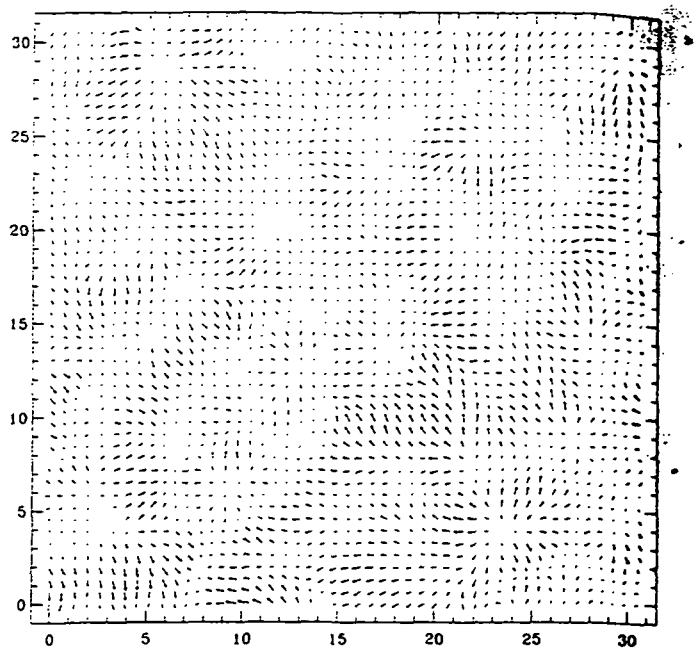

FIG. 3.—Average flow field over all adjacent pairs among the 172 frame WL data set. Each tick mark is 1 arcsec. Maximum vector length corresponds to 1.25 km s^{-1}; rms speed is 0.53 km s^{-1}.

advected to supergranular boundaries and subsequently destroyed, as shown by Muller et al. (1992).

Figure 4 shows the autocorrelation function (ACF) of the velocity field v_x for the WL data. (v_x is plotted here rather than speed, for later comparison with Div and Curl in the next section; all these variables have zero mean, while speed does not.) The ACF of v_x first decreases sharply in the first two minutes and gradually stabilizes after 10 minutes. The sharp drop-off in the first 2 minutes is due to decorrelation of the noise; the 2 minute decorrelation time comes from the inherent time averaging involved in the subfundamental filtering process (Title et al. 1992). The gradual decrease between 2 and 10 minutes is mostly due to evolution of granulation over time. The stable feature after 10 minutes is due to a combination of long-lived solar features such as mesogranulation and supergranulation. This sustained ACF in time of v_x is observed to last for at least a few hours.

4. DIVERGENCE AND CURL

Figure 5 shows the distribution functions of Div and Curl derived from WL flow field. Both distribution functions are Gaussian in nature, but that for Div has a clearly broader distribution than that for Curl. Essentially the same results are seen in the histograms for the GD data, where the difference between Div and Curl is even more pronounced. In the simulation data, the distribution functions for Div and Curl are also Gaussian in shape, but in contrast with the observed data sets, their widths are essentially identical.

As noted earlier, there is nothing in the numerical reduction of the data (see eqs. [1] and [2]) that is likely to introduce a systematic difference if not already pesent in the data. In principle seeing distortions can produce contributions to Div due to lensing, whereas contributions to Curl are much harder to make with wavefront errors. However, since both spatial destretching and time-averaging or temporal filtering successfully remove most of the seeing distortions, such residual effects

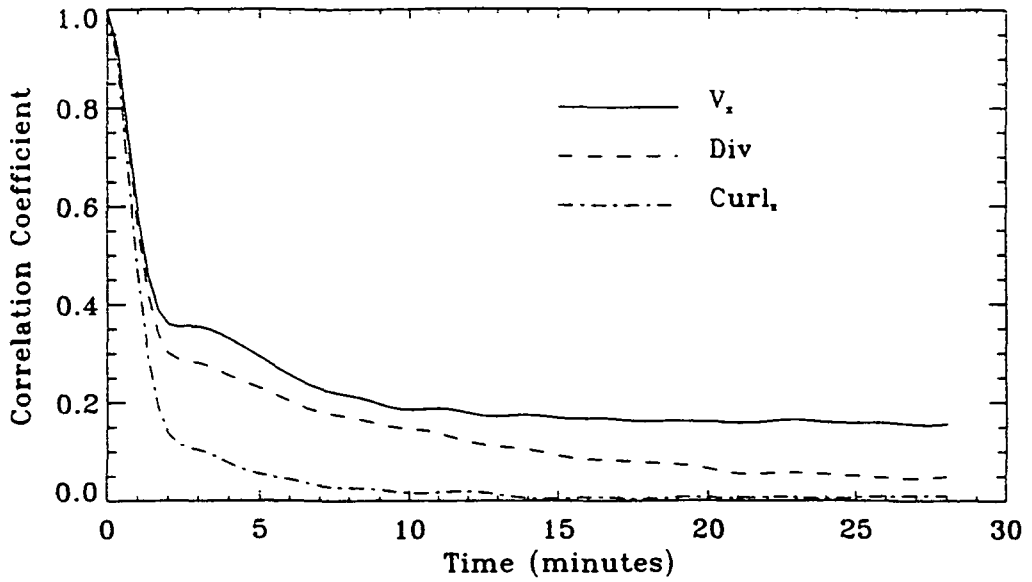

FIG. 4.—Auto-correlation function of v_x, Div, and Curl for the WL series. The sharp dropoff at the beginning is due to decorrelation of noise. The coherence time of v_x is longer than that of Div, which in turn is longer than that of Curl.

should be small. It appears more likely that we are seeing a real property of solar convection that is not captured in the convection simulations.

We have analyzed the auto-correlation function of Div and Curl along with that of v_x, as shown in Figure 4. The rapid decorrelation at the beginning of all three curves is due to noise, as already noted. In contrast to the constancy of the ACF of v_x after 10 minutes due to steady flows at the solar surface, the dashed curve for divergence decreases steadily after 2 minutes, but remains significantly nonzero for at least 30 minutes. In contrast, the dash-dotted curve for Curl drops essentially to zero after 15 minutes. This indicates that at our resolution, Curl has a short lifetime. As we show later in this section, Curl is probably more concentrated in the intergranular lanes with a small spatial scale. We note that the ratio of the ACF of Curl to that of Div is higher for lag times of 2 to 3 minutes than it is at times exceeding 10 minutes. Possibly the contribution of intergranular lanes to the average Curl would contribute to this higher ratio for 2 to 3 minute time lags. Nevertheless, even if we scale Curl to the same level of ACF as that of Div at 2 minutes, the ACF of Curl still drops much faster than that of Div and reaches essentially zero after 15 minutes, and thus does not change our conclusion about the difference between their lifetimes.

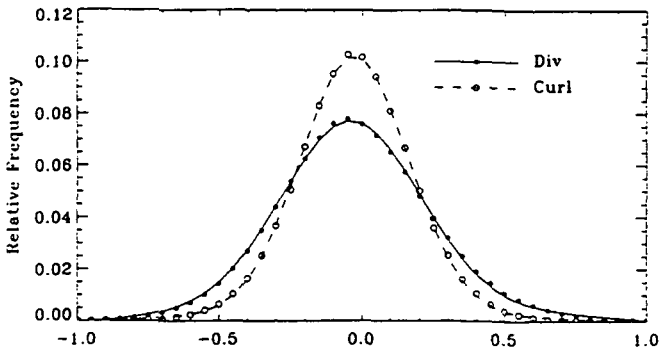

FIG. 5.—Histogram of the values of Curl (*dots*) and Div (*circles*) in the WL data set, together with Gaussian fits to each. The distribution of Div is clearly broader than that of Curl. This is also observed in the GD data set but not in the simulation data.

Figure 6 shows the spatial power spectra of Div and Curl for the WL series. The difference between Div and Curl is evident. The power of Div comes from the diverging flows in the cell centers of mesogranulation and supergranulation and converging flows in the mesogranular and supergranular boundaries. The contribution to Div associated with granules is outside the most reliable part of the data. Compared to Div, the Curl signal has relatively more power at small spatial scales corresponding to downflow regions, as established in the following paragraph. Although our data are not reliable for $k > 1$ Mm^{-1}, they nevertheless suggest that the spatial power of Curl in that range could be at least as much as that of Div. The temporal power spectra of Div and Curl have identical increasing shape with Div having more power at all values ω. These results are all consistent with previously obtained results from the SOUP (Tarbell et al. 1992).

To see how Div and Curl are related to each other, we analyzed the Div and Curl data of the WL series in the following way. There are 171 frames each containing 46^2 values of Div and Curl. We sorted the Div data in increasing order and divided them into 46 bins, each containing $46 \times 171 = 7{,}866$ elements. We calculated the average value of Din within each bin, $\langle \mathrm{Div} \rangle_{\mathrm{bin}}$. Inside each bin, we found values of Curl corresponding to these values of Div and calculated the rms of Curl values, $\mathrm{Curl}_{\mathrm{rms}}$. Figure 7 shows a plot of $\mathrm{Curl}_{\mathrm{rms}}$ versus $|\langle \mathrm{Div} \rangle_{\mathrm{bin}}|$. The absolute value sign indicates the folding of results for $\langle \mathrm{Div} \rangle_{\mathrm{bin}} < 0$ and $\langle \mathrm{Div} \rangle_{\mathrm{bin}} > 0$ for plotting. Values of $\mathrm{Curl}_{\mathrm{rms}}$ within bins of positive values of $\langle \mathrm{Div} \rangle_{\mathrm{bin}}$ (called divergence) are shown with open circles and dashed lines. Solid dots and solid lines represent $\mathrm{Curl}_{\mathrm{rms}}$ in the negative branch $\langle \mathrm{Div} \rangle_{\mathrm{bin}}$ (called convergence). It is apparent in the figure that $\mathrm{curl}_{\mathrm{rms}}$ *has a weak tendency to be larger in regions of convergence*, i.e., regions of downflow. This phenomenon is only marginally significant ($\pm 1\ \sigma$), for each pair of bins with similar $\langle \mathrm{Div} \rangle_{\mathrm{bin}}$; combined over all the bin pairs with $|\langle \mathrm{Div} \rangle_{\mathrm{bin}}| > 0.10$, however, the trend is highly significant. The same asym-

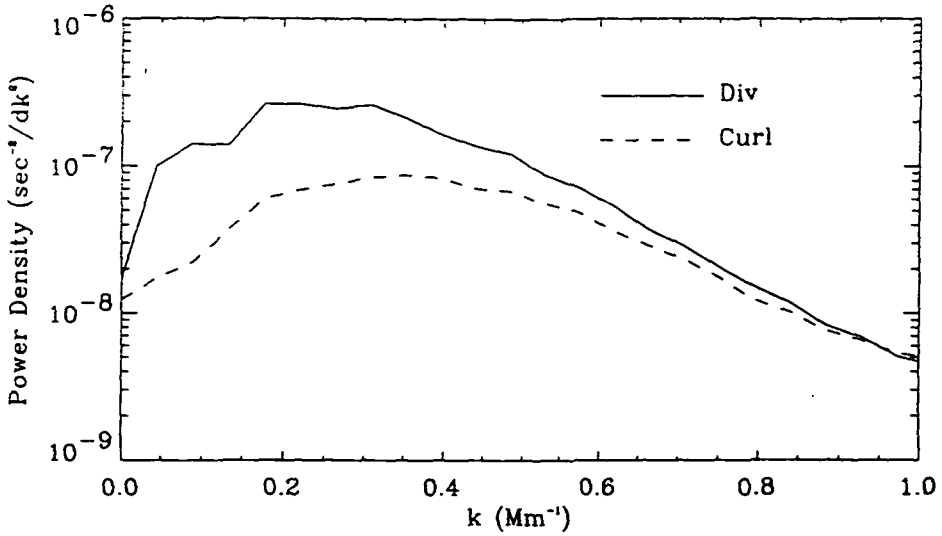

FIG. 6.—Total power density (integrated over all temporal frequencies) of Div and Curl of WL data in the spatial domain. The Div power spectrum dominates at small k. This is because excess power of Div is associated with clearly defined large-scale supergranular, mesogranular and granular structures, while Curl is more concentrated at downflow regions. Thus the power of Curl only matches that of Div at very high spatial frequencies. Units of power density are s^{-2} per $dk^2 = dk_x\,dk_y = (31.2 \text{ arcsec} \times 725 \text{ km arcsec}^{-1})^{-2} = 5.12 \times 10^8 \text{ km}^{-2}$.

metry is also present in the GD data set. The same plot for the simulation data shows the same asymmetry at least at 10 σ level in most ranges of $|\langle \text{Div} \rangle_{\text{bin}}|$ as shown in the lower half of Figure 7.

In the simulation, the Div and Curl have identical spatial and temporal power spectra, differing significantly from the observation. Thus it seems likely that something is going on in the Sun that is not present in the simulation, which gives rise to the above-mentioned differences between Div and Curl. We note again that our numerical calculations of Div and Curl from the flow field differ from each other only in the signs attached to x- and y-components of the flow vectors. Thus it is hard to see how a numerical effect could introduce a false asymmetry in the Div and Curl. While as noted, seeing could more easily introduce an instantaneous contribution to the Div field than to the Curl field, this should not affect analyses involving low temporal frequencies or large time lags in the ACF. Thus it appears that the different behavior of Div and Curl really represent different aspects of the physics of the flow patterns on the Sun.

We have binned the data set in bins of Curl, and made plots of Div_{rms} versus $\langle \text{Curl} \rangle_{\text{bin}}$. Here we found no apparent asymmetry between Div_{rms} in bins with positive or negative Curl_{bin}. This is not surprising since we do not expect a strong preferred sign of rotation at the solar surface. (Rotation-induced Coriolis forces should be negligible given the extremely small granulation and mesogranulation timescales compared to the solar rotation period.) We also plotted $\langle \text{Div} \rangle$ versus $\langle \text{Curl} \rangle_{\text{bin}}$ which shows a Λ shape with roughly the same number of points above and below $\langle \text{Div} \rangle = 0$ line. For high values of $|\langle \text{Curl} \rangle_{\text{bin}}|$, Div is more likely to have a large negative value, i.e., strong convergence. This is consistent with the asymmetry observed in Figure 7 which also implies a stronger association between convergence and Curl than between divergence and Curl.

Shown in Figure 8 are plots of $\langle \text{Div} \rangle$ (*solid dots*) and $\langle \text{Curl} \rangle$ (*open circles*) inside bins of speed for the WL data. The solid line connects points of best polynomial fit to the Div data, while the dashed line is that to the Curl. Error bars are $\pm 1\,\sigma$ of the curve fit. The two curves corresponding to the Div (*solid dots*) and Curl (*open circles*) are significantly different. At very low speed, $\langle \text{Div} \rangle$ is negative. We believe this is due to slow downflows at mesogranular and supergranular boundaries. However, $\langle \text{Curl} \rangle$ averages about zero in the low-speed region indicating no preferred sign of rotation. The general increasing trend of Div at high speed is most probably related to exploding granules whose divergence increases with speed, and whose lifetime can be as long as the time span of the data set. $\langle \text{Curl} \rangle$ remains near zero, once again indicating no preferred sign of rotation. The highest points in both curves are clipped off to keep the noise level down. The 16 frame averaged GD data produces an almost identical graph.

5. ROTATIONAL MOTION OF BRIGHT POINTS

A large number of sub-arcsecond bright points can be found in high-resolution continuum images. They tend to cluster around the supergranular boundaries (Muller et al. 1992). They are typically 0.5 arcsec in size or smaller with mean intensity higher than that of granular centers. Most of these bright points live on the order of a few minutes. However, some can live much longer. We have found a number of bright points that persisted over 30 minutes. They are undoubtedly closely related to the magnetic field. However, the true nature of NBPs awaits future high resolution continuum images with correlated magnetic field data.

We searched for long-lived bright points using space-time slices. They are obtained by slicing the three-dimensional data array in the spatial-temporal plane rather than the x-y plane. The upper part of Figure 9 (Plate 15) shows one of these slices. Granules appear to be bright, elongated broad regions, while bright points appear as thin bright feature surrounded by thin dark lanes. The time slices show occasional wavy bright features within what appear to be intergranular lanes—suggestive of a bright point moving back and forth in x, either due to a horizontal oscillation or perhaps due to circular motion such as a vortex.

Through careful manual screening of the frames, we found that rotational motions of small bright points do occasionally

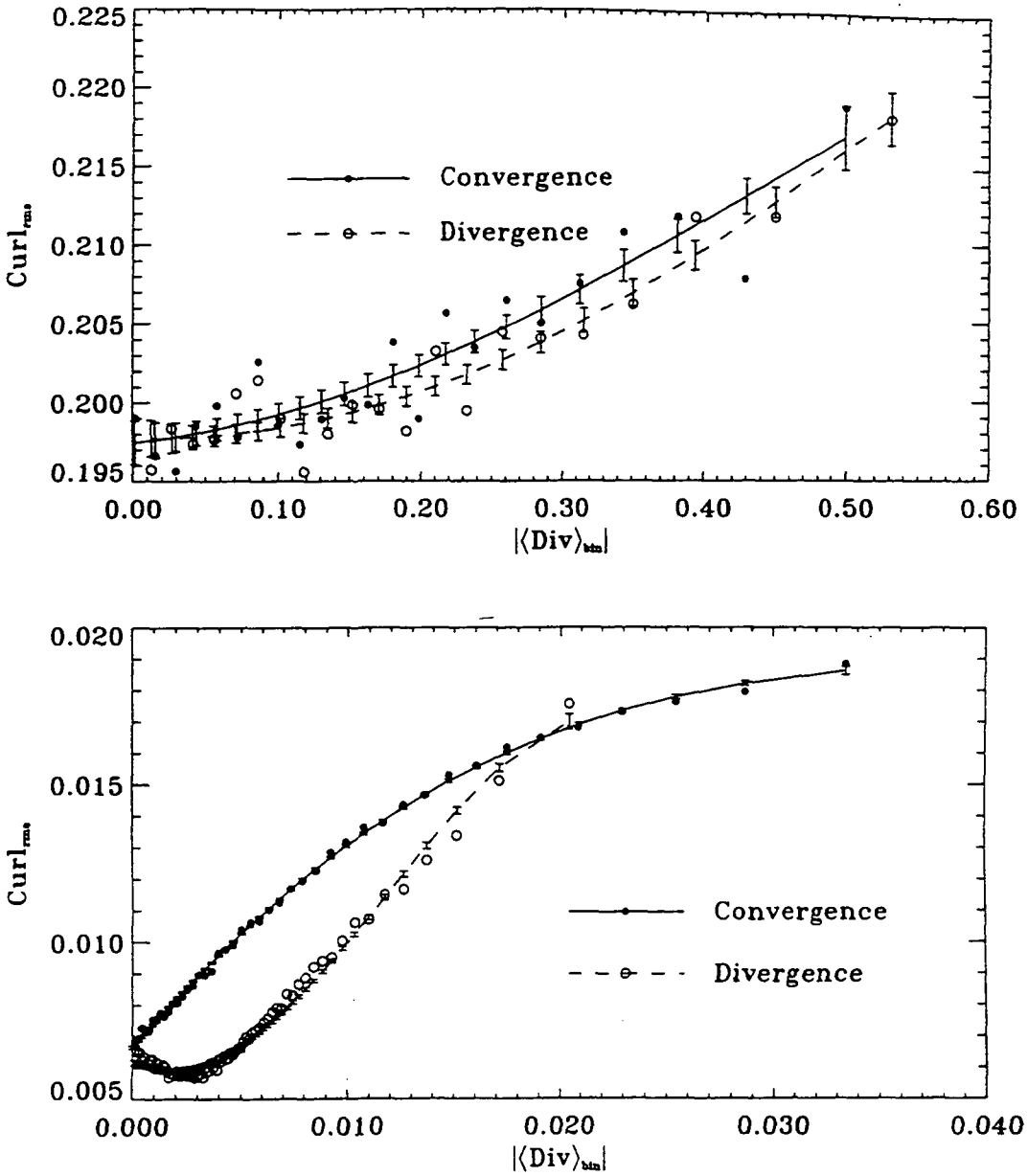

FIG. 7.—Plots of $Curl_{rms}$ vs. $|\langle Div\rangle_{bin}|$ for the WL data (*top*) and the numerical simulation data (*bottom*). In each bin of Div we calculate the average value of Div and the rms of the values of Curl associated with these points. We have folded the axis around zero for display. Solid dots represent $Curl_{rms}$ in bins of Div < 0, with solid lines indicating the best cubic polynomial fit, and error bars indicating $\pm 1\ \sigma$ error to the fit. Open circles and the dashed lines are for $Curl_{rms}$ in bins of Div > 0. The largest value in $Curl_{rms}$ for both curves has been clipped because they are dominated by noise.

occur. An outstanding example is shown in Figure 9, where two small bright points, separated by about 0".65 or 450 km, are seen to rotate about each other at a speed of about 3 km s^{-1}, corresponding to an angular velocity about 1 radian in 160 s, or a period of about 1000 s. The vorticity in this case is about 9 times that of the large vortex observed by Brandt et al. (1988), at $1.3 \times 10^{-2}\ s^{-1}$. However, these rapid rotations are at the limit of our resolution. Numerical simulation indicate that vortex motion is common in downflow regions surrounded by granules though without bright points as tracers, they would not be easily seen. The trend toward large vorticities at small spatial scales is also consistent with the results derived from the medium and low spatial resolution analysis by Simon et al. (1994).

Such clearly defined events proved hard to find. In fact visual search of the WL images resulted in only about a dozen clear bright points whose identity clearly persisted over more than 10 minutes. Most of the small bright points were found to bifurcate or simply disappear after a few minutes, with no clear sign of rotation. We have only one other example where rotation between two bright points can be seen. One problem is the definition of a coordinate system that persists from frame to frame; slight displacements of the frames (even given the prealignment of the frames) can mask motions at the sub-arcsec level. Thus isolated NBP are not a good tracer of local motions because of lack of a good rigid coordinate system. The bright point pair shown in Figure 9 avoids the difficulty, since we can measure relative motions between the two bright points.

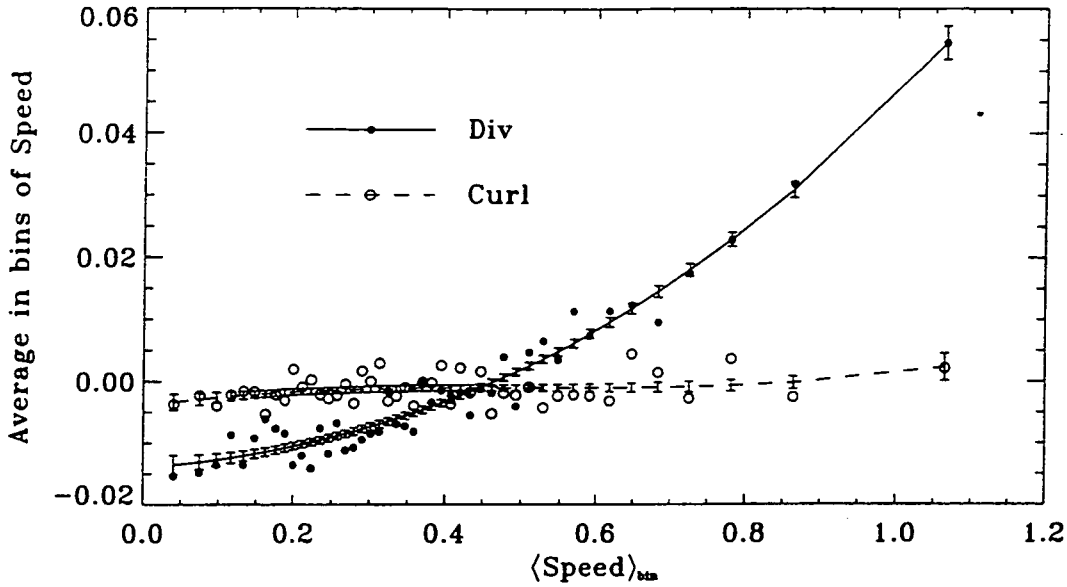

FIG. 8.—Plot of ⟨Div⟩ and ⟨Curl⟩ vs. $\langle \text{Speed} \rangle_{\text{bin}}$ of the WL data. ⟨Div⟩ increases with speed while ⟨Curl⟩ has no such strong trend. The divergence at high speed is thought to be caused by regions of exploding granules where both speed and Div are large. Some of these regions have a lifetime at least as long as 1 hour. The ⟨Div⟩ goes below zero at low speed while ⟨Curl⟩ does not. This difference is probably related to downflow regions at granular, mesogranular, and supergranular boundaries, where convergence is preferred while Curl has no preferred sign.

Another difficulty in studying NBPs arises from the complexity of the dynamics in the field being observed. Motions of granules, exploding granules, surface waves, and other events make it difficult to track these small bright points and their identities are often confusing over time. Space-time slices are very helpful in tracing NBPs. While the bright points can be unclear in image space, the continuity in space-time slices helps preserving their identity.

6. DISCUSSION AND CONCLUSION

The above analyses have shown that Div and Curl of horizontal flow fields in the solar photosphere have distinct characteristics. In summary, we note the following observations.

1. Vorticities seem to have a closer association with inflows than outflows. The asymmetry in our Curl_{rms} versus $|\langle \text{Div} \rangle_{\text{bin}}|$ plot indicates this. This finding is confirmed by the filtered, averaged unfiltered, and simulation data. This extends but is consistent with results others have obtained. Brandt et al. (1988) found a large vortex associated with an inflow region which lasted a few hours. Using a superb set of data from La Palma, Simon et al. (1994) found that at large spatial scales, Curl is associated with downflow regions, and at large temporal scales, vortices can last as long as several hours. Zirker (1993) also found prevalent vorticities in the intergranular lanes, from study of solar convection simulations.

2. Spatial power spectrum of Curl shows higher amplitudes at smaller spatial scales compared with that of Div, and temporal autocorrelation shows that the coherence time of the Curl field is significantly shorter than that of Div. Both numerical simulation and observation of bright points convince us of the fact that the strong vortices exist at granular boundaries, where the spatial and temporal scales are small. The ratio of spatial and temporal power of Curl over Div grows toward smaller spatial and temporal scales, supporting this conclusion. Simon et al. (1994) also observed more power of Curl on smaller scales.

3. High speed is associated with high outflow. We interpret this as the relationship between exploding granules and high divergence. Simon et al. (1991) have pointed out that areas of persistent exploding granules are mesogranular structures seen as diverging regions in time averaged flowmaps. At low speed, we observe convergence which is thought to be associated with inflow at meso- and supergranular scales. Curl has no preferred sign in either high or low speeds, thus averaging to zero.

4. Large local vorticities have been observed. The specific case described here has vorticity 9 times that of Brandt et al. (1988) and 50 times that of Simon et al. (1994). The spatial and temporal scales increase from our observation to that of Brandt, and then to that of Simon. This is consistent with the predictions above.

5. Although in the numerical simulation, the shape of the spatial and temporal power spectra of Div and Curl are essentially the same, they are significantly different in the observed data.

Although not discussed in the text, we have analyzed a set of La Palma data of coarser resolution in exactly the same way as described previously and found the same conclusions as above.

This project was supported by NASA grant NAGW-2545 and the Ford Program for Undergraduate Research at Harvard University; and by NASA contract NASW-4612 and the Independent Research Program at Lockheed. We are very grateful to R. Muller who acquired the outstanding Pic du Midi data set, and to D. H. Porter for providing the simulation data. We thank Neal Hurlburt for useful comments about the simulation data. Y. W. thanks Richard Shine, Zoe Frank, and others at LPARL for their hospitality and assistance during his visit.

REFERENCES

Brandt, P., Scharmer, G., Ferguson, S., Shine, R., Tarbell, T., & Title, A. 1988, Nature, 335, 238
Muller, R. 1990, in Solar Photosphere: Structure, Convection, and Magnetic Fields, ed. J. O. Stenflo (Dordrecht: Kluwer), 85
Muller, R., Auffret, H., Roudier, T., Vigneau, J., Simon, G., Frank, Z., Shine, R., & Title, A. 1992, Nature, 356, 322
Muller, R., & Roudier, T. 1992, Sol. Phys., 141, 27
November, L. J. 1986, Appl. Opt., 25, 392
November, L. J., & Simon, G. W. 1988, ApJ, 333, 427
Porter, D. H., Woodward, P. R., & Mei, Q. 1991, University of Minnesota Supercomputer Institute Research Report Number UMSI 91/150 (Minneapolis: Univ. Minnesota)
Simon, G. W., Brandt, P. N., November, L. J., Scharmer, G. B., & Shine, R. A. 1994, in Solar Surface Magnetism, ed. R. Rutten & C. Schrijver (Dordrecht: Kluwer), 261
Simon, G. W., Title, A. M., Topka, K. P., Tarbell, T. D., Shine, R. A., Ferguson, S. H., Zirin, H., & the SOUP Team. 1988, ApJ, 327, 964
Simon, G. W., Title, A. M., & Weiss, N. O. 1991, ApJ, 375, 775
Sturrock, P. A., & Uchida, Y. 1981, ApJ, 246, 331
Tarbell, T. D., Slater, G. L., Frank, Z. A., Shine, R. A., & Topka, K. P. 1992, in Mechanisms of Chromospheric and Coronal Heating, ed. P. Ulmschneider, R. Rosner, & E. Priest (Berlin: Springer), 39
Title, A., Tarbell, T., Simon, G., & the SOUP Team. 1986, Adv. Space Res., 6, 253
Title, A. M., Tarbell, T. D., Topka, K. P., Ferguson, S. H., Shine, R. A. & the SOUP Team. 1989, ApJ, 336, 475
Title, A. M., Topka, K. P., Tarbell, T. D., Schmidt, W., Balke, C., & Scharmer, G. 1992, ApJ, 393, 782
Topka, K. P., Tarbell, T. D., & Title, A. M. 1986, ApJ, 306, 304
Zirker, J. B. 1993, Sol. Phys., 147, 47
Zirker, J. B., & Cleveland, F. M. 1993, Sol. Phys., 144, 341